Nuclear Materials and Energy 35 (2023) 101446

Contents lists available at ScienceDirect

Nuclear Materials and Energy

journal homepage: www.elsevier.com/locate/nme

Recent progress of plasma exhaust concepts and divertor designs for tokamak DEMO reactors

N. Asakura [a,*], K. Hoshino [b], S. Kakudate [a], F. Subba [c], J.-H. You [d], S. Wiesen [e], T.D. Rognlien [f], R. Ding [g], S. Kwon [h]

[a] National Institutes for Quantum Science and Technology (QST), Naka, Ibaraki 311-0193 Japan
[b] Graduate School of Science and Technology, Keio University, Yokohama 223-8522, Japan
[c] NEMO Group, Politecnico di Torino, Torino, Italy
[d] Max Planck Institute for Plasma Physics, Boltzmannstrasse 2, Garching, Germany
[e] Forschungszentrum Jülich GmbH, Institut für Energie und Klimaforschung Plasmaphysik, 52425 Jülich, Germany
[f] Lawrence Livermore National Laboratory, Livermore, CA, 94551, USA
[g] Institute of Plasma Physics, Chinese Academy of Sciences, Hefei 230031, China
[h] Korea Institute of Fusion Energy, Daejeon 34133, Republic of Korea

ARTICLE INFO

Keywords:
DEMO
Power exhaust
Divertor simulation
Divertor design
Water-cooled divertor

ABSTRACT

The power exhaust concept and an appropriate divertor design are common critical issues for tokamak DEMO design activities which have been carried out in Europe, Japan, China, Korea and the USA. Conventional divertor concepts and power exhaust studies for recent DEMO designs ($P_{\mathrm{fusion}} = 1 - 2$ GW, $R_{\mathrm{p}} = 7 - 9$ m) are reviewed from the viewpoints of the plasma physics issues and the divertor engineering design. Radiative cooling is a common approach for the power fusion scenario. Requirements on the main plasma radiation fraction ($f_{\mathrm{rad}}^{\mathrm{main}} = P_{\mathrm{rad}}^{\mathrm{main}}/P_{\mathrm{heat}}$) and the plasma performance constrain the divertor design concept. Different challenges contribute to optimizing the future DEMO designs: for example, (i) increasing the main plasma radiation fraction for ITER-level $P_{\mathrm{sep}}/R_{\mathrm{p}}$ designs and simplifying the divertor geometry, and (ii) extending ITER divertor geometry with increasing divertor radiation ($P_{\mathrm{rad}}^{\mathrm{div}}$) for larger $P_{\mathrm{sep}}/R_{\mathrm{p}} \geq 25\mathrm{MWm}^{-1}$ designs. Power exhaust simulations with large $P_{\mathrm{sep}} = 150 - 300$ MW have been performed using integrated divertor codes considering an ITER-based divertor geometry with longer leg length (1.6 – 1.7 m), as in a common baseline design. Geometry effects (ITER like geometry or more open one without baffle) on the plasma detachment profile and the required divertor radiation fraction ($f_{\mathrm{rad}}^{\mathrm{div}} = P_{\mathrm{rad}}^{\mathrm{div}}/P_{\mathrm{sep}}$) were key aspects of these studies. All simulations showed that the divertor plasma detachment were extended widely across the target plate with a reduction in the peak heat load of $q_{\mathrm{target}} \leq 10$ MWm^{-2} for the large $f_{\mathrm{rad}}^{\mathrm{div}} = 0.7 - 0.8$, while the peak q_{target} location and value were noticeably different in the partially detached divertor. Simulation results also demonstrated that radial diffusion coefficients of the heat and particle fluxes were critical parameters for DEMO divertor design, and that effects of plasma drifts on outboard-enhanced asymmetry of the heat flux, suggested the need for longer divertor leg to ensure the existence of a detached divertor operation with $q_{\mathrm{target}} \leq 10$ MWm^{-2}.

Integrated design of the water cooled divertor target, cassette body (CB) and cooling pipe routing has been developed for each DEMO concept, based on the ITER-like tungsten monoblock (W-MB) with Cu-alloy cooling pipes. Engineering design adequate under higher neutron irradiation condition was required. Therefore, inlet coolant temperature (T_{cool}) was increased. In current designs, it still shows a large potential variation between 70 °C and 200 °C. The influence of thermal softening on the Cu-alloy (CuCrZr) pipe was fostered near the strike-point when the high q_{target} of $\sim$10 MWm^{-2} was studied. Improved technologies for high heat flux components based on the ITER W-MB unit have been developed for EU-DEMO. Different coolant conditions (low- and high-T_{cool}) were provided for Cu-alloy and reduced activation ferritic martensitic (RAFM) steel heat sink units, respectively. The high-T_{cool} coolant was also considered for the CB and supporting structures. Appropriate conditions for the high-T_{cool} coolant, i.e. 180 °C/ 5 MPa (EU-DEMO) and 290 °C/ 15 MPa (JA-DEMO, CFETR and K-DEMO), will be determined in the future optimizations of the divertor and DEMO design.

---

[*] Corresponding author at: Plasma Theory and Simulation Group, Naka Fusion Institute, QST, 801-1 Mukoyama, Naka, Ibaraki 311-0193, Japan.
E-mail address: asakura.nobuyuki@qst.go.jp (N. Asakura).

https://doi.org/10.1016/j.nme.2023.101446
Received 17 October 2022; Received in revised form 10 April 2023; Accepted 11 May 2023

1. Introduction

Demonstration of electric power production larger than internal power consumption (net electricity generation) is the most outstanding challenge of a DEMO fusion reactor. The fusion power (P_{fusion}) and device size (major radius: R_p) are increased to achieve net electricity generation and tritium breeding to sustain the fusion reactions (self-sufficient tritium breeding). Power exhaust concept and the appropriate divertor design are common critical issues for DEMO tokamak development activities, which have been carried out in Europe (EU-DEMO1 [1,2], Flexi-DEMO [3]), Japan (JA-DEMO 2014 [4,5] and high plasma elongation: high-κ [6]), China (CFETR [7]), Korea (K-DEMO [8,9]), and the USA (FNSF [10], ARIES-ACT1 [11]). Representative plasma parameters and heating power of recent DEMO concepts are shown in Table 1. Those for ITER [12,13] are also added. These plasma parameters are referred to in their cited references. Noted that results of the power exhaust and divertor design in this paper may be taken from other related references, where some design parameters can differ slightly from those representative ones. The EU-DEMO1 baseline design ($R_\mathrm{p}/a_\mathrm{p}$ = 9.0/2.9 m, a_p: midplane minor radius) is considered here, which is referred to as EU-DEMO in the following sections. The power handling concept of the recently proposed Flexi-DEMO ($R_\mathrm{p}/a_\mathrm{p}$ = 8.4/2.71 m, aiming for not only pulsed operation but also steady-state operation if the plasma performance is improved) is similar to the baseline design. Pulsed operation performance was also investigated in the steady-state design of JA-DEMO 2014 ($R_\mathrm{p}/a_\mathrm{p}$ = 8.5/2.4 m). JA-DEMO high-κ (elongation at 95% of a_p: $\kappa_{95} = 1.75$) can increase the plasma current (I_p) with the same device size (R_p and a_p), toroidal field (B_T = 5.9 T) and safety factor (q_{95} = 4.1), which is considered as a reference power exhaust concept in the following sections. For CFETR ($R_\mathrm{p}/a_\mathrm{p}$ = 7.2/2.2 m) and K-DEMO ($R_\mathrm{p}/a_\mathrm{p}$ = 6.8/2.2 m), plasma parameters at the first operational stage are considered. The design activity for FNSF ($R_\mathrm{p}/a_\mathrm{p}$ = 4.8/1.2 m) was recently reviewed, aiming at developing sufficient engineering and technology for tritium breeding ratio (TBR ~ 1.0) and proceeding issues related to net electricity production . A power plant concept from the USA such as ARIES-ACT1 ($R_\mathrm{p}/a_\mathrm{p}$ = 6.25/1.56 m) will achieve above DEMO missions.

Generally, pulsed DEMO concepts have larger P_{fusion}, and steady-state concepts must increase the auxiliary power (P_{aux}) for sufficient plasma current drive. The total heating power (P_{heat}) by α-particles (P_α) and P_{aux} of these DEMO concepts is increased to 1.8 – 3 times larger than that of ITER, while the device size (R_p) is restricted from the ITER-level to 1.5 times larger. A power exhaust parameter of $P_{\mathrm{heat}}/R_\mathrm{p}$ = 39 – 62 $\mathrm{MWm^{-1}}$ noticeably larger than ITER (24 $\mathrm{MWm^{-1}}$) suggests significant increase of the heat flux in the scrape-off layer (SOL) , if radiation losses in the main plasma ($P_{\mathrm{rad}}^{\mathrm{main}}$) are not expected. Double-null divertor design is proposed (K-DEMO, FNSF) or considered (EU-DEMO) for devices with $P_{\mathrm{heat}}/R_\mathrm{p}$ larger than twice that of ITER. The power exhaust scenario and divertor design for the DEMO reactor are critical issues of physics, engineering and technology, and challenges are present even in the conventional approach based on the ITER divertor. During the conceptual design phase, it is important to review the key topics of representative DEMO divertor concepts to facilitate their future improvement and development,even though the reference design concepts of the DEMO reactor, power exhaust and divertor design differ somewhat in each community. Here, we summarize common views and differences in the divertor designs , and clarify critical issues and challenges.

First, the power exhaust scenarios in the main plasma and divertor have been investigated for the various DEMO concepts, while keeping the radiative cooling by impurity seeding as a common approach. The total radiation fraction in the main plasma and divertor is large ($f_{\mathrm{rad}}^{\mathrm{tot}} = P_{\mathrm{rad}}^{\mathrm{tot}}/P_{\mathrm{heat}} \geq 0.8$, where $P_{\mathrm{rad}}^{\mathrm{tot}} = P_{\mathrm{rad}}^{\mathrm{main}} + P_{\mathrm{rad}}^{\mathrm{sol}} + P_{\mathrm{rad}}^{\mathrm{div}}$: total radiation loss in the main plasma, SOL and divertor), compared to that for ITER ($f_{\mathrm{rad}}^{\mathrm{tot}}$ = 0.6 – 0.7) in order to reduce the peak heat load on the divertor target (q_{target}) to 10 $\mathrm{MWm^{-2}}$ level [12,13].

Second, power exhaust simulations in the divertor have been performed by integrated divertor simulation codes to predict a self-consistent transport solution for the plasma, neutrals and impurities in the SOL and divertor. In particular, for the reactor designs, the divertor plasma detachment is required to significantly reduce both the plasma ion and electron temperatures near the strike-points ($T_\mathrm{i}^{\mathrm{div}}$, $T_\mathrm{e}^{\mathrm{div}}$) and the peak q_{target}. Formation of divertor plasma detachment and an operational window in terms of key power exhaust parameters such as exhaust power to the SOL ($P_{\mathrm{sep}} = P_{\mathrm{heat}} - P_{\mathrm{rad}}^{\mathrm{main}}$), radiation loss fraction in the SOL and divertor normalized by P_{sep} ($f^{*\mathrm{div}}_{\mathrm{rad}} = (P_{\mathrm{rad}}^{\mathrm{sol}} + P_{\mathrm{rad}}^{\mathrm{div}})/P_{\mathrm{sep}}$), and characteristic width of the heat flux profile in SOL ($\lambda_\mathrm{q}^{\mathrm{SOL}}$) have been investigated to determine appropriate divertor designs [14–24]. Larger $f^{*\mathrm{div}}_{\mathrm{rad}}$ is required as the divertor power handling parameter ($P_{\mathrm{sep}}/R_\mathrm{p}$) is increased compared to the ITER values ($f^{*\mathrm{div}}_{\mathrm{rad}}$ = 0.5 – 0.6, $P_{\mathrm{sep}}/R_\mathrm{p}$ = 16 $\mathrm{MWm^{-1}}$) [25].

Third, it is also necessary to develop the foreseeable engineering design of the divertor under more severe neutron irradiation conditions compared to ITER. Integrated designs of the water cooled divertor target, cassette and cooling pipe routing have been recently developed for each DEMO concept. The plasma facing components (PFCs) in these conventional divertor designs for DEMO is mostly based on the ITER technology [26], i.e. tungsten monoblock (W-MB) concept with Cu-alloy coolant pipes. Arrangements of the PFCs and coolant pipes for the different DEMO divertor concepts, and common design issues of the water cooled divertor are summarized. Here, design concepts of single-null magnetic geometry and water-cooled divertor are the main focus. Helium (He) cooling target concept is considered for the USA DEMO

Table 1

Key design parameters of recent DEMO concepts, obtained by system codes.

Parameters	EU-DEMO [1,2]	JA-DEMO [4,5]	CFETR (1st stage) [7]	K-DEMO (1st phase) [8,9]	FNSF [10]	ITER (inductive, Q = 10) [12,13]
R_p (m)/ a_p (m)	9.0/ 2.9	8.5/ 2.4	7.2/ 2.2	6.8/ 2.1	4.8/ 1.2	6.2/ 2.0
A	3.1	3.5	3.3	3.2	3.5	3.1
I_p (MA)	18.0	12.3	13.8	12.3	7.9	14
B_T (T)/ $B_\mathrm{T}^{\mathrm{max}}$ (T)	5.9/ 12.5	5.94/ 12.1	6.5/ 14	7.4/ 16	7.5/ 15.9	5.3/ 12
κ_{95}	1.6	1.65	2.0	1.8	2.1	1.7
q_{95}	3.5	4.1	5.5	7.3	6.0	3
Operation	Pulsed 2-hours	steady-state	steady-state	steady-state	steady-state	~ 400 s
Divertor configuration	Single null (option: Double null)	Single null	Single null	Double null	Double null	Single null
P_{fusion} (MW)	2000	1462	974	2200	520	500
P_{aux} (MW)	50	84	82	160	129	73 (installed)
P_{heat}: $P_\alpha + P_{\mathrm{aux}}$ (MW)	457	376	277	600	233	~ 150
$P_{\mathrm{heat}}/R_\mathrm{p}$ ($\mathrm{MWm^{-1}}$)	53	44	39	88	49	24
ave. neutron load to first wall ($\mathrm{MWm^{-2}}$)	~ 1	~ 1	~ 0.7	~ 2	~ 1.2	0.5

divertor. The double-null divertor design is proposed particularly for the large P_{heat}/R_p concept, but it will likely pose significant engineering issues such as installation of the upper divertor coil and restricted remote maintenance. In addition, accurate control of the double-null plasma configuration is required to obtain a balanced up-down divertor power distribution .

This paper reviews the steady-state power exhaust scenario and divertor design development for recent representative DEMO concepts, which were based on a plenary presentation in the 25th International Conference on Plasma Surface Interactions in Controlled Fusion Devices (PSI-25) [27]. Topics were chosen mainly from baseline DEMO design concepts for the steady-state power exhaust, which have been primarily developed for all DEMO concepts. Divertor design for the transient heat load from detached to attached plasma, and developments of the plasma design and relevant equipment for suppressing or mitigating the edge localized mode (ELM) activity are indispensable to finalize the DEMO conceptual design.

Power exhaust concepts for representative DEMO plasma designs are shown in Sec. 2. Section 3 reviews recent status of the power exhaust simulations for DEMO divertor design; simulation codes and input conditions, divertor plasma detachment, divertor geometry, tungsten (W) erosion estimation in the partially detached divertor, and effects of radial diffusion coefficients, are summarized. Engineering design concepts of water-cooled divertor, their issues of high heat removal components and coolant condition, and development of the target technologies are summarized in Sec. 4. Recent progress and key issues are summarized in Sec. 5.

2. Power exhaust concepts with impurity seeding

Power handling in the main plasma is determined by competing requirements of increasing the radiation loss fraction ($f_{rad}^{main} = P_{rad}^{main}/P_{heat}$) vs. the plasma performance as characterized by the enhancement factor of the energy confinement ($HH_{98(y,2)}$) and the normalized β (β_N). Different power exhaust scenarios were proposed for the EU-DEMO and JA-DEMO concepts. Power exhaust concepts were investigated in EU-DEMO [28] and JA-DEMO [6] from the parameter scans by the EU and JA system codes (PROCESS [29] and TPC [30], respectively). Large power exhaust scenarios require radiative cooling both in the main plasma and divertor . Relatively high-Z impurities such as argon (Ar), krypton (Kr) and xenon (Xe) are preferable for the DEMO design [31,32] in order to increase P_{rad}^{main} because of their large radiation loss rate coefficient for high T_e (>100 eV) range as shown in Fig. 2 of Reference [31]. Ar seeding was used as a reference for both DEMOs to control the radiation loss in SOL and divertor, since relatively large radiation loss is expected also at lower T_e (less than 50 eV).

EU-DEMO aims for 2-hours long pulsed operation producing net-electricity of $P_{net} = 500$ MW with $P_{fusion} \sim 2$ GW, which is based on the expected performance of ITER plus conservative improvements in physics and technology. Plasma parameters and the power exhaust concept of the main plasma were shown in Reference [1]: design points of the EU-DEMO ($R_p = 9.0$ m, $B_T \sim 6$ T) were predicted as a function of the P_{sep} ratio above the L- to H-mode transition threshold power [33] ($f_{LH} = P_{sep}/P_{LH}$) while achieving ITER-level $HH_{98(y,2)}$ (1.1) and stable β_N (2.6) by impurity seeding. Minimal R_p (9.0 m) was determined at $f_{LH} = 1.2$ for a given power handling parameter in the divertor ($P_{sep}/R_p = 17$ MWm^{-1}). The plasma density and radiation loss for the baseline design are also shown in Table 2. The EU-DEMO concept challenges increasing f_{rad}^{main} to ~0.67 by impurity seeding scenario with higher-Z impurities such as Kr and Xe, in addition to Ar to employ ITER-level power handling in the divertor, as shown in Fig. 1. Power exhaust parameters of Flexi-DEMO, i.e. $f_{rad}^{main} \sim 0.67$ and $P_{sep}/R_p \sim 20$MWm^{-1} for the pulsed plasma and $f_{rad}^{main} \sim 0.61$ and $P_{sep}/R_p \sim 23$ MWm^{-1} for the steady-state plasma, are also added. Such high f_{rad}^{main} was reported in the ASDEX-Upgrade (AUG) H-mode experiment with Ar and nitrogen (N) seeding [34,35], and some representative values from the database are plotted in Fig. 1. Also reducing the divertor coverage, i.e. removing the divertor baffle, is shown in Secs. 3 and 4 to increase the tritium breeding volume [36].

Table 2
Power exhaust parameters of DEMO concepts with the single null divertor.

Parameters	EU-DEMO [1]	JA-DEMO (higher-κ) [6]	CFETR (steady-state) [20]
line-ave. n_e (10^{19}m^{-3})	8.7	8.6	6.3
n^{GW} (10^{19} m^{-3})	7.2	7.3	9.1
line-ave. n_e/n^{GW}	1.2	1.2	0.67
Seeding (n_{imp}/n_e, %)	Xe (0.039) + Ar	Ar (0.6)	Ar/Ne
P_{heat} (MW)	457	435	305
P_{rad}^{main} (MW)	306	177	86
P_{rad}^{main}/P_{heat}	0.67	0.41	0.28
P_{sep} (MW)	154	258	219
P_{sep}/R_p(MWm^{-1})	17	30	30
$P_{sep}B_T/q_{95}R_pA$ (MWTm^{-1})	9.2	12.5	10.9
P_{LH} in DT(MW)	133	115	68
$f_{LH} = P_{sep}/P_{LH}$	1.2	2.2	3.2

EU-DEMO design points were investigated in Reference. [28] as *figures of merit* for handling transient heat load due to divertor plasma re-attachment and impurity concentration to achieve the divertor plasma detachment. Fig. 3(a) and (b) show the divertor operation boundaries by three thick lines and representative regions; (i) the maximum tolerable heat load condition of $P_{sep}B_T/q_{95}R_pA \sim 9$ MWTm^{-1} (q_{95}: safety factor at 95% of a_p, $A = R_p/a_p$: plasma aspect ratio), (ii) the critical impurity concentration in the SOL to produce divertor detachment ($c_{Z,det}$) comparable to a reference value (c_{REF}), which is consistent with the fuel dilution in the main plasma, and (iii) $P_{sep} = P_{LH}$. Here, the previous design value of $P_{sep} = 150$ MW [1] is assumed for the boundaries (i) and (ii); thus f_{LH} corresponds to 1.36 due to $P_{LH} = 110$ MW [28], where the reference plasma parameters were slightly revised. The normalized $c_{Z,det}$ ($\hat{c}_{Z,det}$) is used in Fig. 2 (a) and (b). Appropriate design points for the divertor operation ($P_{sep}B_t/q_{95}R_pA \leq 9$ MWTm^{-1}) and impurity concentration ($\hat{c}_{Z,det} \leq 1$) are shown within colored area (A and B), where application of the existing superconductor technology corresponds to

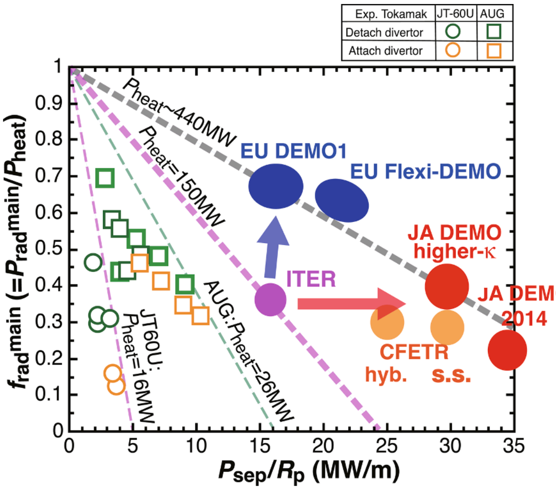

Fig. 1. Fraction of P_{rad}^{main} in the total heating power (P_{heat}) and the divertor power handling parameter (P_{sep}/R_p) for ITER, EU-DEMOs (DEMO1, Flexi-DEMO), JA-DEMOs (DEMO 2014, DEMO higher-κ) and CFETR (hybrid and steady-state concepts). Results of impurity seeding H-mode experiments in AUG [35] and JT-60U [37] are also shown by squares and circles: orange and green colors correspond to attached and detached divertor cases, respectively. (For interpretation of the references to color in this figure legend, the reader is referred to the web version of this article.)

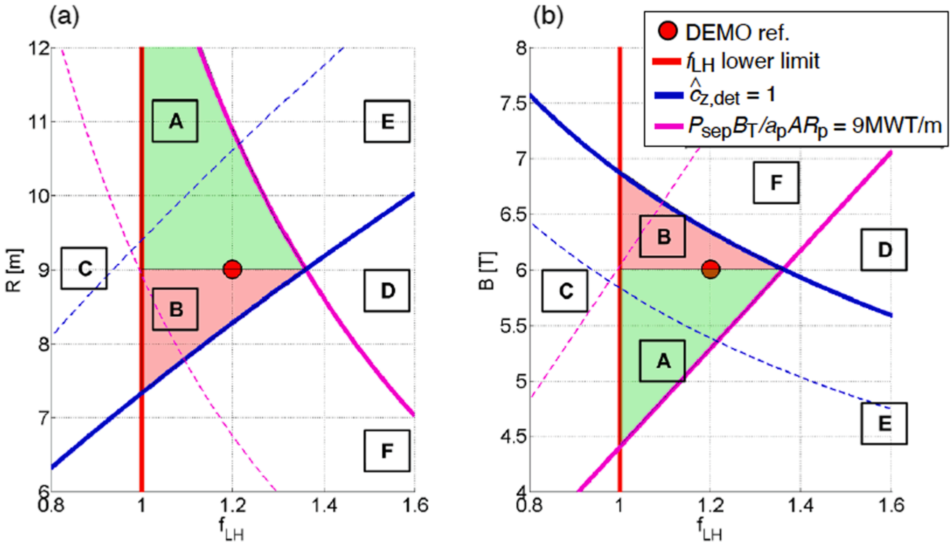

Fig. 2. Constant lines of $P_{sep}B_T/q_{95}R_pA \sim 9$ MWTm^{-1} (blue), $\hat{c}_{Z,det} \leq 1$ (magenta) and $f_{LH} = 1$ (red) in the f_{LH} - R plane (a) and $f_{LH} - B_T$ plane (b) for EU-DEMO study, assuming $P_{fusion} = 2$ GW. The reference design point is represented with a red point ($R_p = 9.0$ m, $B_T = 6$ T, $f_{LH} = 1.2$). Green shaded areas "A" identify the feasible EU-DEMO configurations, the red shaded areas "B" identify the configuration which would be feasible if advanced superconducting magnetic technology (a higher magnetic field in a smaller space than current one) is provided. C, D, E, F are not suitable for reactor operation: (C) below P_{LH}, (D) both figures of merit, (E) excessively high impurity concentration, (F) unable to deal with loss of detachment by divertor sweep and ITER-like target technology. [28]. (For interpretation of the references to color in this figure legend, the reader is referred to the web version of this article.)

"A". Provided that $f_{LH} = 1.2$ is a standard value for EU-DEMO concept, design point for updated EU-DEMO corresponds to $P_{sep}B_T/q_{95}R_pA \sim 8.11$ MWTm^{-1} and $\hat{c}_{Z,det} = 0.85$, and the exhausted power is reduced to $P_{sep} = 132$ MW. Noted that the ambiguity of P_{LH} is relatively small from the power threshold database in low Z_{eff} region (< 2) [33], which is relevent to the ITER. However, further improvement of the database with regard to impurity seeding and P_{LH} scaling for higher Z_{eff} will be necessary to determine P_{LH} more acculately for the DEMO plasma designs

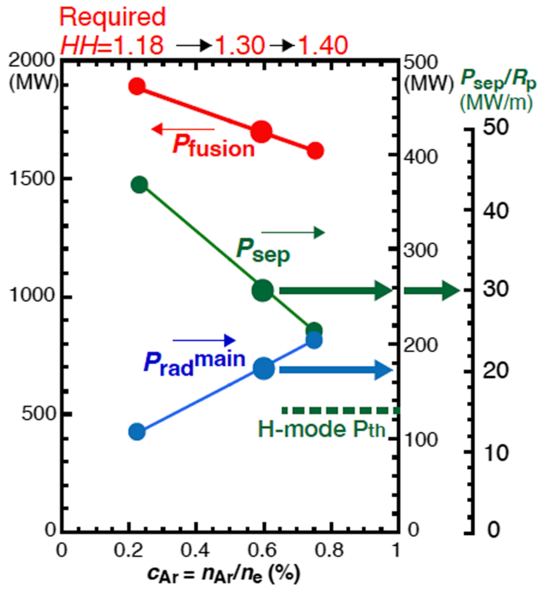

Fig. 3. P_{fusion} (red), P_{rad}^{main} (blue), P_{sep} (green) as a function of Ar impurity concentration ($c_{Ar} = n_{Ar}/n_e$) for JA-DEMO with increasing $\kappa_{95} = 1.75$. $HH_{98(y,2)}$ required for $\beta_N = 3.4$ is increased with increasing c_{Ar}. P_{rad}^{main} includes radiation loss power due to bremsstrahlung, synchrotron and impurity line radiations. Power handling parameter for the divertor (P_{sep}/R_p) is also shown at the right axis. Design point of JA-DEMO higher-κ is shown in large circles ($c_{Ar} = 0.6\%$). P_{LH} (114 MW) is shown by dotted line. [6]. (For interpretation of the references to color in this figure legend, the reader is referred to the web version of this article.)

JA-DEMO aims to steady-state operation producing P_{net} of a few 100 MW with $P_{fusion} \sim 1.5$ GW and installing enough central solenoid (CS) coils for full inductive plasma start up. High plasma density is required to achieve adequate power exhaust and low fuel dilution by impurities. For the primary plasma design (JA-DEMO 2014) as shown in Table 1, high Greenwald density fraction of $f^{GW} = \bar{n}_e/n^{GW} = 1.2$ ($n^{GW} = I_p/\pi a_p^2$ [10^{20} m^{-3}, MA, m]) was assumed, thus I_p and the line-averaged density ($\bar{n}_e$) were restricted to 12.3 MA and 7.9x10^{19} m^{-3}, respectively. Further increase of c_{Ar}^{main} reduced P_{fusion} below 1.5 GW due to the fuel dilution, and, at the same time, $HH_{98(y,2)} > 1.3$ was required. Therefore, c_{Ar}^{main}, P_{rad}^{main} and f_{rad}^{main} were restricted up to 0.25%, 82 MW and 0.22, respectively.

JA-DEMO higher-κ design (κ_{95} is increased from 1.65 to 1.75) increased I_p to 13.5 MA and $\bar{n}_e$ to 8.6×10^{19} m^{-3}, and also improved the plasma performance such as P_{fusion} and τ_E. Thus, the baseline requirements ($HH_{98(y,2)} = 1.3$, $\beta_N = 3.4$) for the steady-state JA-DEMO plasma can be obtained under the higher impurity condition of $c_{Ar}^{main} = 0.6$ %, as shown in Fig. 3 and Table 2: P_{heat} becomes comparable to that of EU-DEMO, P_{rad}^{main} is substantially increased from 82 MW (DEMO 2014) to 177 MW, and P_{sep} is reduced from 294 MW to 258 MW, which provides enough margin above P_{LH} ($f_{LH} = 2.2$). Therefore, the power exhaust concept of $f_{rad}^{main} \sim 0.4$ with $HH_{98(y,2)} = 1.3$ (both are slightly higher than ITER-level) and large P_{sep}/R_p (~30MWm^{-1}) are performance challenges for both the main plasma and divertor. The power exhaust parameters for both JA-DEMO designs are shown in Fig. 1, where some representative results of $f_{rad}^{main} \sim 0.4$ and detached divertor experiments in JT-60U long-pulse with Ar seeding were plotted [37]. Here, vertical stability of the high κ_{95} plasma was sustained by passively induced current in the conducting structures without in-vessel control coils. Increasing κ_{95} from 1.65 to 1.75 required improvements of the conducting shell design such as increasing the electrical conductance (shell width) and installing an additional shell behind the inboard breeding blankets (BBs) [38].

Since the n^{GW} values for both JA- and EU-DEMO designs are lower than that of ITER (1.1x10^{20} m^{-3}), H-mode operation with high $f^{GW} > 1$ is required to satisfy appropriate P_{fusion} and P_{net} values. On the other hand, recent experiments (JET-ILW and AUG) reported the restriction at high-f^{GW} (0.9–1) to obtain H-mode plasmas only by external gas fueling [39]. A relatively peaked profile of n_e and a pedestal density of less than n^{GW} will be necessary for the JA- and EU-DEMO plasmas to obtain the high

f^{GW}, and an internal transport barrier (ITB) of the T_e and T_i profiles as well as the n_e profile will need to be maintained, in particular, for the JA-DEMO plasma to achieve higher $HH_{98(y,2)}$ and β_N.

The plasma performance for the first target of the CFETR steady-state scenario was proposed in Reference [20], with a focus on tritium breeding; $P_{fusion} \sim 1$ GW, a stable β_N (2.0), and high $HH_{98(y,2)}$ (1.4) at relatively low $\bar{n}_e$ (6.2×10^{19} m^{-3}) and f^{GW} (0.67), which challenges the high-κ plasma design actively controlled by in-vessel coils. Power exhaust results are shown in Table 2. Power handling of large P_{sep} (219 MW) and P_{sep}/R_p (30 MWm^{-1}) is required in the divertor due to low f_{rad}^{main} (0.28), as shown in Fig. 1. Further improvement of β_N (~3.0) will achieve a high bootstrap current fraction ($f_{BS} \sim 0.75$) at a DEMO level performance of $P_{fusion} \sim 2$ GW with increasing $\bar{n}_e$ up to n^{GW}. In addition, the corresponding hybrid operation scenario with ohmic heating fraction of 0.3, aiming at reducing slightly $HH_{98(y,2)}$ (~1.2) and increasing $\bar{n}_e$ ($f^{GW} = 0.85$) for the comparable P_{fusion}, reduces P_{sep} (177 MW) and P_{sep}/R_p (25 MWm^{-1}) with the same f_{rad}^{main}.

The first phase of the K-DEMO ($R_p = 6.8$ m, $P_{fusion} = 2.2$ GW) steady-state concept was proposed to increase $f_{rad}^{main} \sim 0.4$ in order to handle the large $P_{heat} \sim 600$ MW [22] and to achieve the high plasma performance with high f_{BS}, i.e. $HH_{98(y,2)} = 1.2$, $\beta_N = 2.8$, $f_{BS} = 0.77$ [9]. The FNSF long pulse scenario proposed relatively low $f_{rad}^{main} = 0.24$ for $HH_{98(y,2)} \sim 1$, $\beta_N = 2.6$, $f_{BS} = 0.52$ [10]. While P_{sep} (360 MW for the K-DEMO and 177 MW for the FNSF) was different, P_{sep}/R_p became large (53 and 37 MWm^{-1}, respectively), which were respectively 3.3 and 2.3 times larger than that of ITER. Thus, the double-null plasma configuration was chosen for these two designs to distribute the large P_{sep} to the upper and lower divertors.

Consequently, in the recent DEMO-level power exhaust with P_{heat} of 2 – 4 times larger than that of ITER, the exhaust scenario of the large thermal power both in the main plasma and divertor is a common high priority issue. Representative concepts of increasing f_{rad}^{main} with the high plasma performance ($HH_{98(y,2)}$, β_N, f_{BS}) are summarized for the DEMO missions, which determine power handling in the divertor. At the same time, designs need to provide adequate performance for power handling and particle exhaust in the relatively low density DEMO plasmas. Design improvement to high plasma density is required from the viewpoints of reduction in the fuel dilution and the power exhaust in the main plasma and divertor.

3. Power exhaust simulation for DEMO divertor design

3.1. Divertor simulation codes and conditions

Conventional designs of DEMO divertors have been developed, based on the ITER divertor. Large power handling of $P_{sep}/R_p \sim 30$ MWm^{-1} is an important challenge for JA-DEMO and CFETR, and similar size of a long leg divertor ($L_{div} = 1.6 – 1.7$ m, i.e. 1.6 – 1.7 times longer than ITER) is proposed as shown in Fig. 4 (a) and (b), respectively. For the JA-DEMO divertor, the poloidal angle between the separatrix and target surface at the strike point (θ^{div}) is designed as 30° and 25° at the inner and outer targets, respectively. The flux expansion along the target, i.e. $f_{exp}^{div}/sin\theta^{div}$ where $f_{exp}^{div} = (B_p/B_T)^{mid}/(B_p/B_T)^{div}$, is similar at the inner and outer targets (~12). The divertor PFC encloses all plasma below the X-point, and the SOL field lines within the outer midplane radius (r^{mid}) of 4 cm is contacted to the inner and outer divertors. The outer target angle of CFETR is smaller than those of the JA-DEMO and ITER, thus compression of the neutral particles and efficient formation of plasma detachment will be expected particularly near the strike-point. The design concept of the ITER divertor is simplified for the EU-DEMO, i.e. baffles are removed and targets encloses near the strike-points of the long divertor leg, in order to increase the tritium breeding volume. The open and shallow geometry is considered as shown in Fig. 4(c). Instead of the dome structure, a shielding liner is installed in the private region to cover the exhaust opening against neutron flux.

Divertor plasma performance has been simulated mainly with Ar impurity seeding for DEMO. Fig. 4 also shows calculation mesh for the divertor simulations of SONIC on the JA-DEMO divertor (Ar) [14], SOLPS5.0 on the CFETR divertor (Ne or Ar) [20], and SOLPS-ITER on the EU-DEMO divertor (Ar) [17]. As will be shown in Sec. 3.3, UEDGE is used for FNSF with Ne seeding, and for K-DEMO to compare N_2, Ne and Ar seeding. Plasma cross-field drift modelling was not used (not incorporated in SONIC) for these simulation results. Studies of longer leg divertor including drifts effects on the CFETR divertor were performed by SOLPS-ITER [21], and both the inner and outer leg lengths were recently extended (1.6 m and 2.4 m, respectively). For the EU-DEMO simulation, the shielding liner is removed in this simulation work. Exhaust power (P_{out}) and particle flux were given at the core–edge boundary ($r^{mid}/a = 0.95$ for JA-DEMO and CFETR, and 0.98 for EU-DEMO); $P_{out} = 250$, 200, 150 MW for the above reference cases, and $P_{sep} \sim 235$, 193, 146 MW, respectively, which were slightly smaller than P_{out} since the radiation loss in the plasma edge is less than 7% of P_{out}.

Selection of the radial diffusion coefficients (diffusivities) on the ion and electron heat fluxes (χ_i, χ_e) and particle flux (D) for the SOL plasma

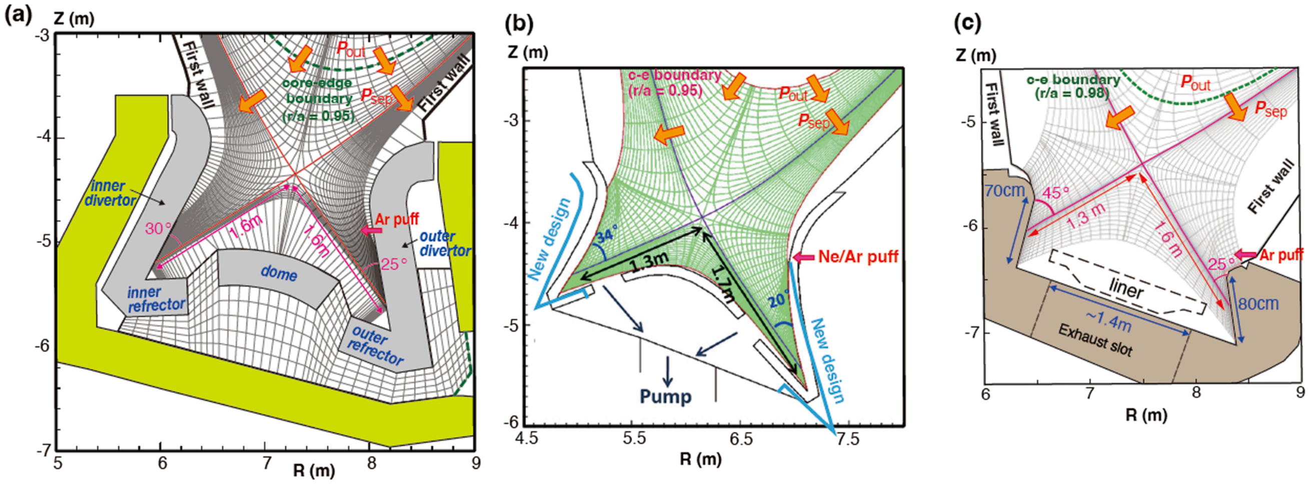

Fig. 4. (a) SONIC simulation mesh for the plasma fluid and neutral/impurity MC calculation, and the divertor geometry of JA-DEMO [14]. (b) SOLPS5.0 simulation mesh for the plasma fluid calculation, and the divertor geometry of CFETR [29]. It is used also for SOLPS-ITER simulation. (c) SOLPS-ITER simulation mesh for the plasma fluid calculation, and the divertor geometry of EU-DEMO [17].

Table 3
Power exhaust and diffusion coefficients of DEMO divertor simulation.

Parameters	EU-DEMO [17]	JA-DEMO [6,14]	CFETR [20]	FNSF[23]
Divertor code	SOLPS-ITER	SONIC	SOLPS5.0	UEDGE
P_{sep} (MW)	~ 146	~ 235	~ 193	~ 88 (lower divertor)
T_e^{sep} (keV)	0.2	0.37	0.46	~ 0.2
T_i^{sep} (keV)	0.5	0.83	2.1	~ 0.5
n_e^{sep} (10^{19} m^{-3})	2.8	2.0	1.7	~ 6
$\chi^{edge/SOL}$ (m^2 s^{-1})	0.2/ 0.18 (*1)	1.0	1.0	0.5
$D^{edge/SOL}$ (m^2 s^{-1})	0.2/ 0.42 (*1)	0.3	0.3	0.33
$\lambda_{q//}^{mid}$ (mm)	~ 3	2.9	~ 3	~ 2

Note *1: The former and latter values are provided for edge and SOL regions, respectively.

is a critical issue to simulate the divertor performance. Representative power exhaust parameters and diffusion coefficients are summarized in Table 3. For the JA-DEMO, $\chi_i = \chi_e = 1$ m^{2}s^{-1} and $D = 0.3$ m^{2}s^{-1} were the same as the "standard" values of ITER simulation by SOLPS4.3 [40]. The e-folding length near the outer midplane separatrix ($\lambda_{q//}^{mid}$) of the parallel heat flux ($q_{//}$) profile (including electron and ion components) corresponded to 2.9 mm, which was narrow compared to 3.6 mm in the ITER simulation due to higher T_e^{sep} and T_i^{sep} in the JA-DEMO (370 and 830 eV, respectively). The same $\chi = 1$ m^{2}s^{-1} and smaller $\chi = 0.2 – 0.18$ m^{2}s^{-1} were given for CFETR and EU-DEMO, respectively. While local $\lambda_{q//}^{mid}$ become small than 2 mm for the latter case, average $\lambda_{q//}^{mid}$ near the separatrix ($\Delta r^{mid} < \sim 1$ cm in SOL) is provided to similar value of ~3 mm. For the UEDGE simulation on the FNSF divertor [22], the half power of P_{sep} (0.5x176 MW) was assumed to be transported to the lower divertor and use of smaller $\chi = 0.5$ m^{2}s^{-1} provided smaller $\lambda_{q//}^{mid} \sim 2$ mm. On the other hand, $\lambda_{q//}^{mid}$ was estimated by $\lambda_{q//}^{Eich} = 0.7 \cdot B_t^{-0.77} \cdot q_{95}^{1.05} \cdot P_{sep}^{0.09}$ [mm, T, MW] [41] based on the experimental database of heat load profiles under the attached divertor condition, and the scaling predicted $\lambda_{q//}^{Eich} = 0.9$ and 1.2 mm for ITER and JA-DEMO, respectively. Similar to the ITER case, $\lambda_{q//}^{mid}$ used for DEMO simulations was also wider than the empirical scaling. Reductions of both χ and D by factors of 2 and 4 produced smaller $\lambda_{q//}^{mid}$ of 1.6 and 1.2 mm, respectively, in ITER simulations [40] and the peak $q_{//}$ became larger. On the other hand, increase of the peak q_{target} remained comparatively small (20 – 40 %) due to enhancement of the particle recycling near the divertor separatrix. The influence of reducing the radial diffusion coefficients for the JA-DEMO simulation is shown and discussed in Sec. 3.5.

3.2. Plasma detachment and divertor operation at low density

A simple formula for the target heat load by the plasma (q_t^{plasma}) is described by P_{sep}, f^{*div}_{rad}, $\lambda_{q//}^{mid}$ and the flux expansion along the target ($sin\theta^{div}/f^{div}_{exp}$), as follows: $q_t^{plasma} = (P_{sep}/R_p) \cdot (1\text{-}f^{*div}_{rad}) \cdot (sin\theta^{div}/f^{div}_{exp}) \cdot (4\pi\lambda_{q//}^{mid}D^{det})^{-1}$, where the power reduction in the detachment is represented by a dissipation factor (D^{det}). Integrated divertor simulation provides a two dimensional transport solution of the plasma, neutrals and impurities in the divertor. P_{sep}, f^{*div}_{rad} and radial diffusion coefficients are important key parameters for the divertor performance. In particular, for the large P_{sep}/R_p DEMO designs, larger f^{*div}_{rad} is required compared to that of ITER (0.5–0.6). Simulation scans will determine the appropriate divertor size and geometry to maintain the large radiation peak in the divertor chamber. At the same time, n_e^{sep}/n^{GW} was reported to be ~1/3 in the H-mode plasma experiments [42,43] and a similar fraction in "standard" ITER simulations [40]. Recent experimental results in AUG W-wall and JET-ILW were also lower than critical values of 0.4 – 0.5 [44], which was predicted from the edge ballooning models, i.e. ballooning parameter formula assuming the critical ballooning parameter of 2.0 – 2.5. As a result, the operation range of n_e^{sep}/n^{GW} is expected to be 0.3 – 0.5, thus the operation boundary will be investigated in the density range of $n_e^{sep} = 2 – 3.5\times10^{19}$ m^{-3}, which is lower than that of ITER. Representative JA- and EU-DEMO results are mainly shown as different power exhaust concepts and divertor geometries.

Divertor operation in the low n_e^{sep} range and the influences of key parameters were recently investigated in JA-DEMO [14]. A series of n_e^{sep} scan was performed with changing fuel gas puff and divertor pumping rates (2 – 10$\times10^{22}$ Ds^{-1}), where the Ar seeding rate was controlled to keep a fixed f^{*div}_{rad} value. Two reference series for "JA-DEMO higher-κ" (Case-1: $P_{sep} \sim 235$ MW and $f^{*div}_{rad} \sim 0.8$) and "JA-DEMO 2014" (Case-2: $P_{sep} \sim 283$ MW and the same f^{*div}_{rad}), and the more severe condition with reduced f^{*div}_{rad} of ~0.7 for the two references (Case-3 and Case-4) were investigated. The power exhaust parameter above, $P_{sep} \cdot (1\text{-}f^{*div}_{rad})$, corresponds to 50, 60, 75 and 90 MW for Cases 1 to 4, respectively. Fig. 5(a) and (b) show distributions of the radiation power density (W_{rad}) in the inner and outer divertors at $n_e^{sep} = 2.0\times10^{19}$ m^{-3} for Case-1, corresponding to a near lower boundary of the n_e^{sep} range. The total radiation powers in the inner and outer divertors are comparable, i.e., 79 MW and 82 MW, respectively. The large radiation peaks near the separatrix are maintained at the upstream on both divertor legs.

In the inner divertor, a large W_{rad} is seen at 40 – 60 cm poloidally upstream of the target near the separatrix, and it is maintained far above the inner target. T_e is decreased to ~1 eV over most of the area of the target, which we describe as "full detachment", as shown in Fig. 5 (c). The total heat load (q_{target}) is evaluated by including surface recombination of the ions ($q_t^{rec} = n_i^{div}C_s^{div}E_{ion}$, where n_i^{div}, C_s^{div} and E_{ion} are ion density, sound velocity at the divertor sheath and recombination energy, respectively), radiation power load (q_t^{rad}) and neutral flux load including charge exchange and volume recombination processes (q_t^{n}), in addition to the plasma heat flux (q_t^{plasma}). Multi-peaks appear near the strike-point in the q_{target} profile as shown in Fig. 5 (e), which are attributed to peaks of the n_e^{div}, n_i^{div}, T_e^{div} and T_i^{div} profiles. The largest peak q_{target} of 4.2 MWm^{-2} is seen in the detached region, mostly attributed to q_t^{rec}.

In the outer divertor, a large W_{rad} is also seen at the upstream (40 – 60 cm) near the separatrix, where local c_{Ar} ($= n_{Ar}/n_i$) is increased up to 2 %. On the other hand, the W_{rad} peak shifts toward the target at the outer flux surfaces as shown in Fig. 5 (b), and it becomes smaller than 10 MWm^{-3} (lowest color bar) and located just above the target (a few cm). The plasma detachment is produced on the target within ~12 cm near the strike-point as shown in Fig. 5 (d), which we describe as "partial detachment". The peak q_{target} of 5.5 MWm^{-2} is seen at the boundary of the attached region, where both T_e^{div} and T_i^{div} are increased from ~1 eV to ~15 eV, and n_e^{div} is decreased from ~ 1.5$\times10^{22}$ m^{-3} to ~ 1.5$\times10^{21}$ m^{-3}. Thus, the peak q_{target} is sensitive to their profiles. At the same time, since the W_{rad} peak shifts toward the target, q_t^{plasma} and q_t^{rad} become dominant in the q_{target}. In the partial detachment, the peak q_{target} is sensitive to the plasma temperature and density profiles and location of the W_{rad} peak.

The outer peak q_{target} is generally larger than that of the inner peak q_{target}. Divertor operation for the outer peak q_{target} in the low n_e^{sep} range and the influences of key parameters were summarized in Fig. 6. Closed circles show a n_e^{sep} scan for Case-1, where the reference shown in Fig. 5 is marked by open circle. Squares, triangles and diamonds show other three n_e^{sep} scans for Case-2, Case-3 and Case-4, respectively. The peak q_{target} is reduced with increasing n_e^{sep}, and increased with increasing $P_{sep} \cdot (1\text{-}f^{*div}_{rad})$. As a result, Case-1 and Case-2 have acceptable solutions in the low range ($n_e^{sep} \sim 2\times10^{19}$ m^{-3}) to reduce $q_{target} \leq 10$MWm^{-2}. On the other hand, for Case-2, the peak q_{target} is increased from 5.6 MWm^{-2} (Case-1) to 9.5 MWm^{-2} at $n_e^{sep} = 2\times10^{19}$ m^{-3} with reduced radial width of the plasma detachment to 10 cm on the target. Since the surface temperature of the W target is reduced in Case-1 (JA-DEMO higher-κ), compared to Case-2 (JA-DEMO 2014), it has advantages to provide enough operation margin to the recrystallization temperature (~1200 °C). For the lower $f^{*div}_{rad} \sim 0.7$ cases (Case-3 and Case-4), the detachment width is further decreased, and the peak q_{target} is seen also at the attached region. The peak q_{target} is further increased to 12.2 and 14.5

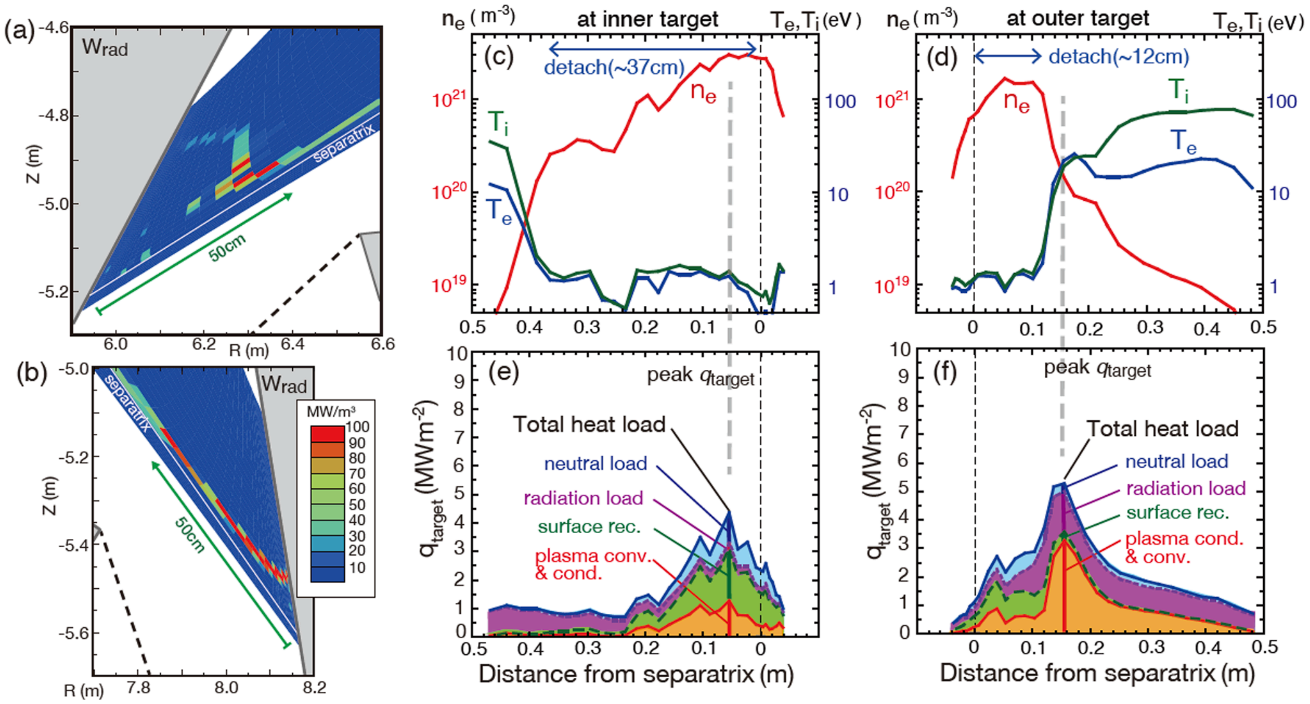

Fig. 5. (a)(b) Distributions of Ar radiation power density (W_{rad}) in the inner and outer divertors, respectively: $n_e^{\mathrm{sep}} = 2.0 \times 10^{19}\mathrm{m}^{-3}$, $P_{\mathrm{out}} = 250$ MW, $P_{\mathrm{rad}}^{\mathrm{edge}} + P_{\mathrm{rad}}^{\mathrm{sol}} + P_{\mathrm{rad}}^{\mathrm{div}} = 200$ MW and $P_{\mathrm{sep}} = 235$ MW. Profiles of (c) (d) n_e^{div}, T_e^{div} and T_i^{div}, (e)(f) integrating heat load components as functions of radial distance along the inner and outer divertor targets, respectively. [14].

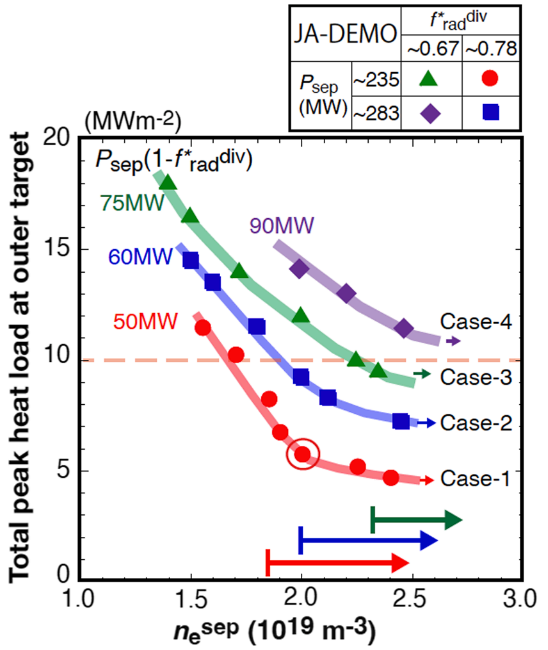

Fig. 6. Four series of peak q_{target} at the outer target for given exhaust power (P_{sep}) and radiation fraction in the SOL and divertor ($f^{*\mathrm{div}}_{\mathrm{rad}} = (P_{\mathrm{rad}}^{\mathrm{sol}} + P_{\mathrm{rad}}^{\mathrm{div}})/P_{\mathrm{sep}}$) as a function of n_e^{sep} [14]. Circles and squares show Case-1 (red); JA-DEMO higher-κ reference ($P_{\mathrm{sep}} \sim 235$ MW, $f^{*\mathrm{div}}_{\mathrm{rad}} \sim 0.8$) and Case-2 (blue); JA-DEMO 2014 reference ($P_{\mathrm{sep}} \sim 283$ MW, the same $f^{*\mathrm{div}}_{\mathrm{rad}}$). Triangles (green) and diamonds (purple) show Case-3 and Case-4, respectively, i.e. lower $f^{*\mathrm{div}}_{\mathrm{rad}}$ (~0.7) cases corresponding to Case-1 and Case-2, respectively. (For interpretation of the references to color in this figure legend, the reader is referred to the web version of this article.)

MWm^{-2} at $n_e^{\mathrm{sep}} \sim 2\mathrm{x}10^{19}$ m^{-3} due to the increase in q_t^{plasma}, where both the local T_e^{div} and T_i^{div} are increased. Higher n_e^{sep} operation (>$2.3\mathrm{x}10^{19}$) is acceptable for Case-3, and further high n_e^{sep} ($2.6 – 3.0\times10^{19}$ m^{-3}) will be required for Case-4. For all cases, Ar concentrations in the midplane SOL ($c_{\mathrm{Ar}}^{\mathrm{sep}} = n_{\mathrm{Ar}}^{\mathrm{sep}}/n_e^{\mathrm{sep}}$) are reduced to 0.4 – 1% for the range of $n_e^{\mathrm{sep}} = 2.0 – 2.5\times10^{19}$ m^{-3}.

Divertor plasma performance for the EU-DEMO divertor has been investigated, using SOLPS-ITER. Reductions in T_e^{div} and q_{target} were investigated by increasing the Ar seeding rate ($0.2 – 2\times10^{21}$ $\mathrm{Ar\cdot s}^{-1}$) at relatively large gas puff rates such as an order of 10^{23} $\mathrm{D\cdot s}^{-1}$. The radiation loss distribution in the divertor, plasma profiles and accumulated heat load profiles in the inner and outer targets for the representative results are shown in Fig. 7, where $n_e^{\mathrm{sep}} \sim 2.8\mathrm{x}10^{19}$ m^{-3} is higher than that of the JA-DEMO and the Ar seeding rate is 1.5×10^{21} $\mathrm{Ar\cdot s}^{-1}$. P_{sep} is 146 MW, which is slightly less than P_{out} of 150 MW. Total line radiation is 75 MW, and the distribution in the divertor is shown in Fig. 7 (a). While $f^{*\mathrm{div}}_{\mathrm{rad}} = 0.51$, it is noted that neutral dissipation processes by charge exchange and recombination processes become 49 MW related to the large fuel gas puff. Thus, total volumetric energy loss from the plasma becomes 0.85 of P_{sep}. Large W_{rad} is seen along both the inner and outer divertor legs near the separatrix. In the inner divertor, T_e^{div} is 0.4 – 3.5 eV as shown in Fig. 7 (b): detachment ($T_e^{\mathrm{div}} \leq 1$ eV) is produced over a substantial region. The peak q_{target} (3.2 MWm^{-2}) appears at $r^{\mathrm{div}} \sim 3$ cm, where q_t^{n} becomes largest contribution near the strike-point (~1.2 MWm^{-2}) as well as q_t^{rec} (~1 MWm^{-2}). At the same time, q_t^{rad} (0.3 – 0.9 MWm^{-2}) is extended in a wide region due to large W_{rad} extended above the inner target. On the other hand, in the outer divertor, partial detachment is produced inside $r^{\mathrm{div}} \leq 6$ cm, and T_e^{div} is increased up to 24 eV in the attached region as shown in Fig. 7 (d). It is noted that peak q_{target} (3.2 MWm^{-2}) appears in the detached region ($r^{\mathrm{div}} \sim 4$ cm), where the local T_e^{div} is ~1 eV. Therefore, q_t^{plasma} is significantly decreased for the EU-DEMO simulation, and both q_t^{rec} (1.3 MWm^{-2}) and q_t^{n} (1.1 MWm^{-2}) are dominant, compared to q_t^{plasma} and q_t^{rad} (0.4 – 0.5 MWm^{-2}). These values of q_t^{plasma}, q_t^{rec} and q_t^{rad} are similar to those in the detached region of the JA-DEMO result such as at $r^{\mathrm{div}} \sim 3$ cm in Fig. 5 (f). Since q_t^{n} for the EU-DEMO is 2 – 3 times larger, dissipation of momentum

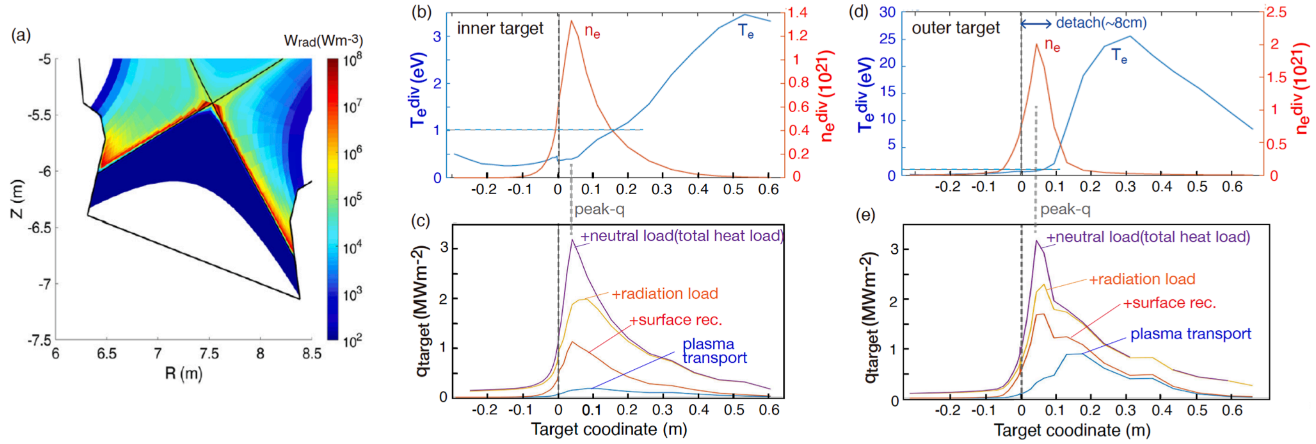

Fig. 7. (a) Distribution of line radiation power density in the divertor for EU-DEMO simulation. (b) (d) Profiles of n_e^{div} and T_e^{div}, (c) (e) Profiles of integrating heat load components at the inner and outer divertor target, respectively [17]. Radial coordinate for the heat load profiles (c) (e) is adjusted to that for the plasma profiles (b) (d). Vertical thick dotted lines correspond to the heat load peak locations, and horizontal thin dotted lines show $T_e^{div} = 1$ eV.

and ion flux may be enhanced in the EU-DEMO result. Comparison between the two divertors by either SONIC or SOLPS-ITER code, or benchmarking between SONIC and SOLPS-ITER codes in either divertor case will be required. In addition, in the EU-DEMO result, the peak q_t^{plasma} (~1 MWm^{-2}) appears in the attached region ($r^{div} = 13 – 18$ cm) similar to that in the JA-DEMO case, while local q_{target} (1.6 – 1.9 MWm^{-2}) is lower than the peak q_{target}. Since the q_t^{plasma} is sensitive to the T_e^{div} and n_e^{div} profiles in the partial detached divertor, investigation of the radial diffusion on the plasma profile is important as well as that of the plasma dissipation models.

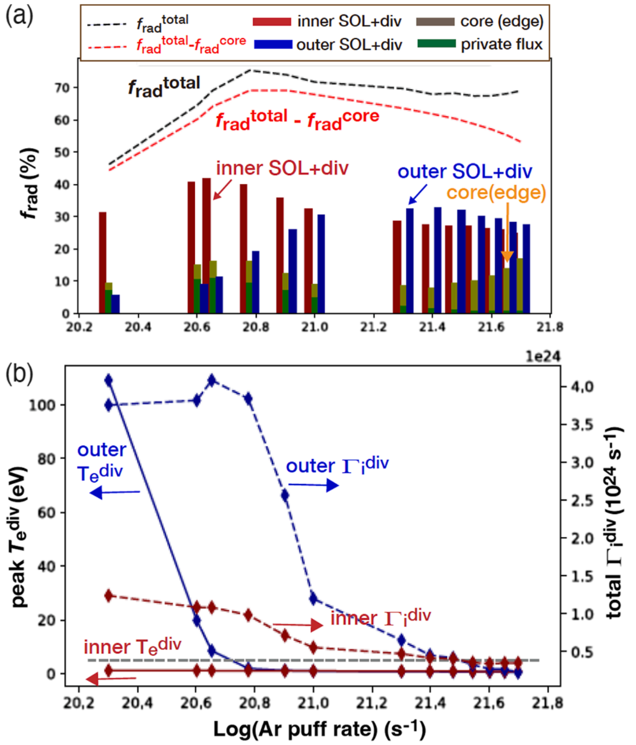

Fig. 8. (a)Vertical bars show radiation power fractions in the different plasma regions in inner SOL + divertor (dark red), outer SOL + divertor (blue), private flux (green), and core (between core–edge boundary and separatrix: dark yellow) regions, as a function of Ar seeding rate. Dotted lines show total radiation fractions of $f_{rad}^{total} = (P_{rad}^{edge} + P_{rad}^{sol} + P_{rad}^{div})/P_{out}$ and $(P_{rad}^{sol} + P_{rad}^{div})/P_{out.}$ (b) Integrated ion fluxes (dash lines) and peak T_e^{div} (solid lines) at the inner and outer targets. Dark red and blue colors correspond to inner and outer SOL + divertor regions, respectively. The ion flux at the outer target begins to reduce as the peak T_e^{div} drops below 5 eV (horizontal dotted line). [19]. (For interpretation of the references to color in this figure legend, the reader is referred to the web version of this article.)

The systematic study of plasma detachment was recently performed by SOLPS-ITER code with higher $n_e^{sep} \sim 4\times10^{19}$ m^{-3} assuming larger ion flux by pellet fueling at the core–edge boundary [19]. Peak T_e^{div} at the outer target is reduced with increasing Ar seeding rate as shown in Fig. 8 (b), and the detachment in the outer divertor is produced at Ar seeding rate of 6×10^{20} $Ar\cdot s^{-1}$. At the same seeding rate, the total radiation fraction (f_{rad}^{total}) also reaches the maximum as shown in Fig. 8 (a). In this study, f_{rad}^{total} is normalized by P_{out} (150 MW) and P_{rad} in the edge plasma (described as "core") is ~17 % of P_{out}, thus the maximum $f_{rad}^{total} \sim 0.75$ corresponds to $f^*{}_{rad}^{div}$ [$= (P_{rad}^{total} - P_{rad}^{edge})/P_{sep}$] ~ 0.70. Power loss by neutral dissipation processes is not included. Since the ion flux to the target is significantly decreased with further increasing the Ar seeding rate, large radiation loss is not maintained in the divertor region, and $f^*{}_{rad}^{div}$ (and f_{rad}^{total}) is gradually decreased due to increasing P_{rad} in the edge plasma. As a result, $f^*{}_{rad}^{div}$ is increased efficiently up to ~0.7 with increasing the Ar seeding to ~6×10^{20} $Ar\cdot s^{-1}$. Further Ar seeding increases c_{Ar} and P_{rad} in SOL and edge regions, while the radiation loss in the divertor is reduced and large radiation peak is shifted towards the X-point. Thus, the detachment is enhanced both in the inner and outer divertors.

3.3. Effects of divertor geometry and drifts

Vertical target design was applied for the ITER divertor from the viewpoints of producing the plasma detachment near the separatrix at lower n_e^{sep} and the wider operation range without building up the X-point MARFE [45]. Since year-long level steady-state operation is expected for the DEMO divertor, reductions of peak T_e^{div} (and T_i^{div}) as well as the peak q_{target} are required to minimize erosion of the W-target under the partial detached divertor.

The effects of target angle (θ^{div}) on the detachment plasma and peak q_{target} were investigated in the FNSF divertor by the UEDGE code with neutral/gas fluid modelling [23]. The vertical target geometry ($\theta^{div} = 25°$) was a baseline design similar to ITER, and the inner and outer L_{div} were 0.37 m and 0.60 m, respectively. Further open geometries ($\theta^{div} = 50°$ and 70°), where the flux expansion at the target was decreased, were compared as shown in Fig. 9 (a). Lower divertor performance was simulated with a half power of P_{sep}, i.e. 88 MW. Thus, only the ITER-level power handling parameter ($0.5P_{sep}/R_p = 18$ MWm^{-1}) was required in the shorter leg divertor. Ne seeding was used, and relatively high n_e (1×10^{20} m^{-3}) was given at the core–edge boundary ($r^{mid}/a_p = 0.97$). The total radiation fraction by neon (Ne) and hydrogen isotopes

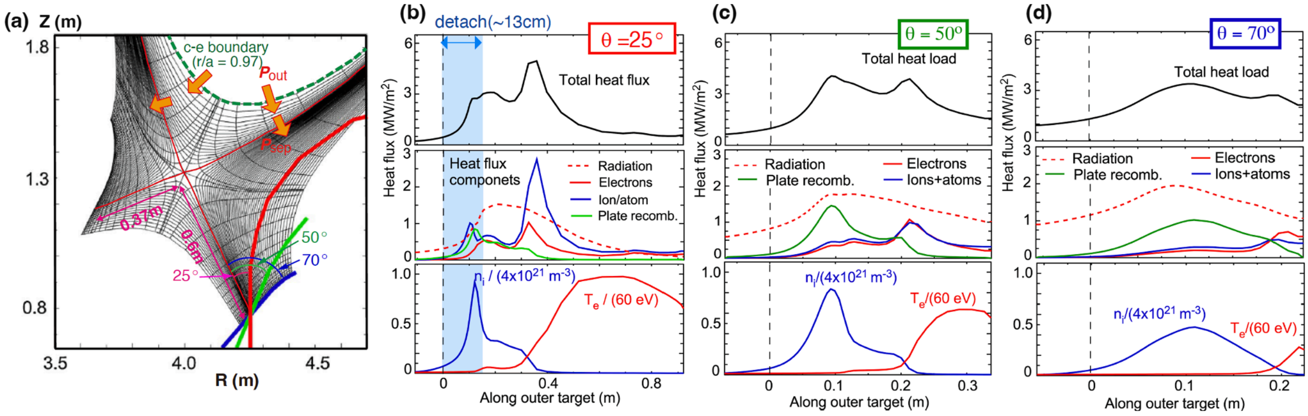

Fig. 9. (a) UEDGE calculation mesh for a baseline divertor design (vertical target geometry; $\theta^{\text{div}} = 25^{\circ}$), and other open target geometries ($\theta^{\text{div}} = 50^{\circ}$ and 70°) [23]. (b) Baseline design result at the outer target: (upper frame) total heat load along the outer divertor plate, (middle frame) heat load components of radiation, electron heat flux, ion and neutral heat flux including charge exchange and recombination processes, and surface recombination, (lower frame) profiles of electron density and temperature. Results of open target cases with poloidal angle at the strike point of (c) $\theta^{\text{div}} = 50^{\circ}$ and (d) $\theta^{\text{div}} = 70^{\circ}$ are shown.

(D/T) corresponds to $f^{*\text{div}}_{\text{rad}} = P^{\text{div-low}}_{\text{rad}}/(0.5P_{\text{sep}}) = 0.83$. For the baseline case, Fig. 9 (b) shows that partial detachment is produced at the outer target, and that low peak q_{target} ($\sim$5 MWm^{-2}) can be sustained in the attached region ($r^{\text{div}} \sim 0.3$ m), which is attributed mainly to $q_{\text{t}}^{\text{plasma}}$ ($\sim$4 MWm^{-2}). Relatively high $T_{\text{e}}^{\text{div}}$ of $\sim$60 eV is seen in the outer region (r^{div} = 0.5 – 0.7 m) as shown in the lower plot of Fig. 9 (b). Here, heat load components by electron and ion/atom transports are separately shown in the middle plot of Fig. 9 (b), and the ion/atom transport component includes charge exchange and volume recombination processes (q_{t}^{n}). In addition, another peak q_{target} ($\sim$3 MWm^{-2}) is seen in the detach-attach boundary (r^{div} = 0.13 – 0.25 m), where $T_{\text{e}}^{\text{div}}$ = 2 – 3 eV and $q_{\text{t}}^{\text{rad}}$ ($\sim$1.5 MWm^{-2}) is the major heat load compared to the other components ($q_{\text{t}}^{\text{plasma}}$, q_{t}^{n}, and $q_{\text{t}}^{\text{rec}}$) due to significant radiation peak near the target. It was noted [23] that kinetic transport modelling of neutrals and molecules (self-consistent coupling of the UEDGE and DEGAS codes) is required for accurate evaluation, which would be expected to extend the low $T_{\text{e}}^{\text{div}}$ region and further reduce the peak q_{target}.

For the open geometry cases ($\theta^{\text{div}} = 50^{\circ}$ and 70°), the detached region becomes radially wider, and the peak q_{target} at the attached region is reduced due to reduction in $T_{\text{e}}^{\text{div}}$ (and $T_{\text{i}}^{\text{div}}$) as shown in Fig. 9 (c) and (d). For both cases, $q_{\text{t}}^{\text{rad}}$ is also the major heat load component. For the case of $\theta^{\text{div}} = 50^{\circ}$, the peak q_{target} in the detach-attach boundary (r^{div} = 0.10–0.18 m) is increased due to increase in $q_{\text{t}}^{\text{rec}}$, and the two peak q_{target} values are comparable ($\sim$4 MWm^{-2}). For the case of $\theta^{\text{div}} = 70^{\circ}$, the detached region is widely extended to $r^{\text{div}} \sim 0.18$ m, and $T_{\text{e}}^{\text{div}}$ and $T_{\text{i}}^{\text{div}}$ are further reduced to less than 1 eV. A broad q_{target} peak ($\sim$3.5 MWm^{-2}) is seen near $r^{\text{div}} \sim 0.1$ m, where $q_{\text{t}}^{\text{rad}}$ ($\sim$1.8 MWm^{-2}) is the major heat load, then $q_{\text{t}}^{\text{rec}} \sim 1$ MWm^{-2}, and $q_{\text{t}}^{\text{plasma}}$ is reduced to $\sim$0.7 MWm^{-2}. It is similar to the inner divertor (nearly full detachment). The operation window of wide detachment and low q_{target} is important for the choice of the divertor geometry. At the same time, transport modelling of dissipation processes, elastic collisions and kinetic effects become important to evaluate the peak q_{target} and the impurity distribution in the nearly fully detached divertor. Further studies will continue using self-consistent simulation of the UEDGE and DEGAS2 codes.

Appropriate divertor leg length (L_{div}) for the vertical target design is primarily determined to maintain the seeding impurity and large radiation peak in the divertor. Divertor performance with L_{div} = 1.6 – 1.7 m has been investigated for the high $P_{\text{sep}}/R_{\text{p}}$ handling such as JA-DEMO (30 – 35 MWm^{-1} by Ar seeding) [14,15] and CFETR (28 MWm^{-1} by Ne seeding) [20], and these results were demonstrated to be appropriate for their reference design. Further study was recently performed for the CFETR by SOLPS-ITER with various drifts activated such as$\nabla B \times \boldsymbol{B}$ and $\boldsymbol{E} \times \boldsymbol{B}$, which produced inboard-enhanced asymmetry of the particle flux profile and outboard-enhanced heat load profile for the normal B_{T} direction, i.e. ion∇B drift towards the divertor [21]. Extension of L_{div} was proposed, and effects on the plasma detachment and impurity retention in the divertor were investigated. Geometries of the refence and longer leg divertors are shown in Fig. 4 (b) and 10 (a): both inner and outer L_{div} were extended from 1.3 m and 1.7 m to 1.6 m and 2.4 m, respectively. Here, inner θ^{div} was increased from 34° to 46°, and outer θ^{div} was the same (20°) [46]. P_{out} from the core–edge boundary was the same (200 MW) as the previous study, but radial distributions of χ and D were introduced, where χ was reduced to 0.5 m^{2}s^{-1} inside the separatrix (r^{mid} = -5 – 0 cm) and increased to 2.0 m^{2}s^{-1} in the far SOL region (r^{mid} = 3 – 6 cm): D was similarly varied. Typical $\lambda_{q//}^{\text{mid}}$ was $\sim$4 mm and $n_{\text{e}}^{\text{sep}} = 3.7\times10^{19}$ m^{-3} in the series of calculations. Comparison between Ne and Ar seedings showed that divertor cooling by the Ar seeding was efficient, thus the Ar seeding was chosen for the baseline scenario.

Under a comparable conditions for the gas puff (4×10^{22} D·s^{-1}) and Ar seeding (4×10^{19} Ar·s^{-1}) with drifts activated, the poloidal distributions of T_{e} and c_{Ar} near the separatrix from the outer midplane SOL to the target for the two leg length cases are compared in Fig. 10 (b) and (c), respectively. For the reference case, the target plasma becomes attached ($T_{\text{e}}^{\text{div}}$ = 230 eV) due to lower radiation loss in the outer divertor, while $T_{\text{e}}^{\text{div}}$ is significantly reduced to $\sim$3 eV for the longer leg case. Next, similar poloidal distributions of T_{e} are achieved with increasing Ar seeding (1×10^{20} Ar·s^{-1}) only for the reference case as shown in Fig. 10 (d) and (e), where $f^{*\text{div}}_{\text{rad}} \sim 0.7$ is comparable and similar partial detachment ($T_{\text{e}}^{\text{div}} \sim 1$ eV) is produced near the separatrix (Fig. 10 (f) and (g)). For the longer leg case, peak $T_{\text{e}}^{\text{div}}$ at $r^{\text{div}} \sim 0.35$ m in the attached region is reduced from 47 eV (reference case) to 34 eV while reduction in the peak q_{target} is small. As a result, drifts will affect the divertor performance, i.e. more severe heat load and higher peak $T_{\text{e}}^{\text{div}}$ at the outer divertor, the longer leg is considered as new baseline design in order to reduce both the peak q_{target} and $T_{\text{e}}^{\text{div}}$, to produce required c_{Ar} in SOL and edge regions, and to extend the divertor operation window at lower $n_{\text{e}}^{\text{sep}}$.

Reduction in the peak q_{target} by N$_2$, Ne or Ar seeding was investigated in the double-null divertor for K-DEMO (by UEDGE) [22] with ITER-level leg length and larger power to either divertor, i.e. $0.5P_{\text{out}}$ = 300 MW. Results showed that Ar seeding enhanced partial detachment more than Ne and N$_2$ cases, and the peak q_{target} was efficiently reduced. It is noted that appropriate power handling ($q_{\text{target}} \leq 10$ MWm^{-2}) was achieved only by reducing the pumping speed, i.e. increasing the albedo of the divertor pumping to 0.99945. Since the operation window of the detachment is limited, further improvements of the geometry and the power exhaust scenario both in the main plasma and divertor will be required.

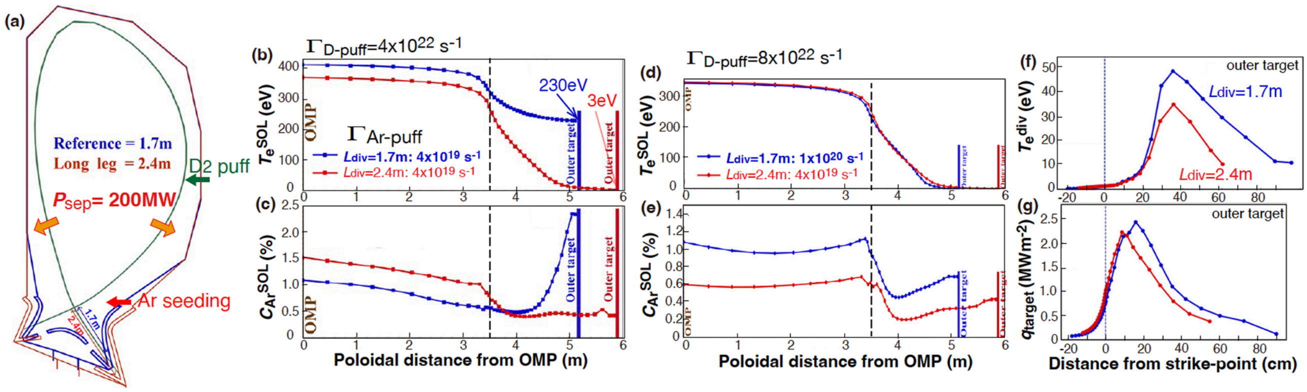

Fig. 10. (a)Baseline (reference) and long leg divertor geometries for CFETR. SOLPS-ITER simulations with various drifts activated such as$\nabla B \times \boldsymbol{B}$ and $\boldsymbol{E} \times \boldsymbol{B}$ [21]. Comparisons of poloidal profiles (starting from the outer midplane down to outer target) of (b) electron temperature (T_e^{SOL}) and (c) Ar concentration (c_{Ar}^{SOL}) near the separatrix ($r - r_{sep} = 0.1$ cm mapped to OMP), for the reference and long leg divertors. For both cases, D_2 gas injection rate and Ar seeding rate are 4.0x10^{22} and 4.0x10^{19} atom s^{-1}, respectively. Comparisons of poloidal profiles of (d) T_e^{SOL} and (e) $c_{Ar}{}^{SOL}$ near the separatrix from the OMP to outer target with the same Ar seeding rate and D_2 gas injection rate of 8.0x10^{22} atom s^{-1}. Ar seeding rate for reference divertor and longer leg divertors are 1.0x10^{20} and 4.0x10^{19} atom s^{-1}, respectively. Corresponding radial profiles of (f) T_e^{div} and (g) total heat load (q_{target}) along the outer target.

3.4. *Estimation of steady-state W-erosion in the partial detachment*

Net erosion of the W target becomes a life-time issue for the DEMO divertor since the ion fluence is expected to be one order of magnitude larger than that in ITER. Low T_e^{div} and T_i^{div} plasma is preferable in the partially detached divertor, in particular, for the vertical target geometry. W-flux sputtered from the target was reported in addition to the divertor plasma parameters of EU-DEMO [17], JA-DEMO [14], CFETR [20] and FNSF [23], where these estimations were carried out by different methods. W-sputter flux and simple estimation of the erosion rate are summarized in Table 4. Here, effects of transient plasma flux such as mitigated ELMs are not included as we described in Sec. 1. W-erosion is enhanced mainly by seeding impurity at the attached region, where the local T_e^{div} is increased to 20 – 40 eV while the incident ion flux (Γ_i^{div}) is reduced at the outer r^{div}. Gross W-sputter flux in the DEMO divertor simulation is sensitive to local plasma condition of Γ_i^{div} and impurity concentration (c_Z) as well as T_e^{div}. Typical values of gross W-sputter flux (Γ_W^{div}) are reported to be a wide range between 6.3×10^{17} and 8×10^{19} W·m^{-2}s^{-1}, where the TRIM code surface database [47] was used for the EU-DEMO result (the small one) and the DIVIMP code (including prompt redeposition and self-sputtering of W) [48] was applied to the CFETR (the high one). For the JA-DEMO case, Γ_W^{div} was determined mostly by Ar impurity ions, and it was defined as yields per impacting hydrogen ion ($Y_Z \cdot c_Z \cdot \Gamma_i^{div}$) [42], where the incident energy for the suppering yield (Y_Z) was given by the typical charge state (Z), plasma temperatures and the sheath potential, i.e. $2Z \cdot T_i^{div} + 3T_e^{div}$. For the FNSF case, Y_Z was calculated by the incident plasma ions (D/T) with the temperatures and the sheath potential, i.e. ($2T_i^{div} + 3T_e^{div}$) [49].

Table 4
Estimation of W erosion depth at the peak T_e^{div} by seeding impurities.

	EU-DEMO [17]	JA-DEMO [6,14]	CFETR [20]	FNSF[23]
T_e^{div} *at* r^{div} (attached region)	20 eV at 40 cm	25 eV at 20 cm	20 eV at 45 cm	40 eV at 45 cm
Γ_i^{div} (m^{-2}s^{-1})	~ 10^{21}	4x10^{22}	5x10^{21}	~ 10^{22}
$c_Z = n_Z/n_i$ (%)	1 (Ar)	0.4 (Ar)	0.6 (Ne)	0.4 (Ne)
Γ_W^{div} (m^{-2}s^{-1})	6.3x10^{17} (*1)	1.9x10^{19}	8x10^{19}	7x10^{18}
Net erosion ratio: R_{net}	0.1	0.1	0.03 (*2)	0.1 (*3)
Δd_{sec} (nm s^{-1})	~ 0.001	0.03	0.04	0.011
Δd_{year} (mm year^{-1})	~ 0.03	~ 0.9	~ 1.2	~ 0.3

Note *1: calculation is performed using the TRIM database [47].
Note *2: Ratio is evaluated by DIVIMP calculation [48].
Note *3: prompt re-deposition reduction factor is chosen from [50].

Net erosion rate is estimated by a simple formula of Δd_{sec} (nm/s) = $10^3 \cdot R_{net} \cdot \Gamma_W^{div}/[6.02\times10^{26}/183.8 \cdot \rho] = 1.57\times10^{-20} R_{net} \cdot \Gamma_W^{div}$, where R_{net} is the ratio of net to gross erosion rate and ρ is W mass density (19.3×10^3 kgm^{-3}). R_{net} is also a critical factor, and 0.1 is given for the FNSF estimation, which considers prompt redeposition (finite-Larmor) effect [50]. The same R_{net} is assumed for the EU-DEMO and JA-DEMO cases, and lower value of 0.03 is evaluated by DIVIMP calculation for the CFETR case. Prompt and local deposition modelling such as the finite-Larmor effect and friction force by the plasma flow, and an experiment database for gross to net erosion ratio are urgently needed. Net erosion depth for year-long operation is also estimated as Δd_{year} (mm/year) = $4.95\times10^{-19} R_{net} \cdot \Gamma_W^{div}$, which is an order of magnitude larger than that of ITER (e.g. assuming ITER with 2500 pulses of 400 s discharges per year). Some results suggest that Δd_{year} reaches the 1 mm-level, which corresponds to 10 – 20% of the monoblock thickness. As a result, simulation results in the vertical target geometry suggested further reduction of both peak T_e^{div} and T_i^{div}, such as "pronounced detachment" reported in ASDEX-upgrade [35], where the peak T_e^{div} ~ 5 eV in the partially attached region, is preferable. Operation at higher n_e^{sep} and/or sweep of the strike-point location [28,51] will need to be considered.

3.5. *Effects of radial diffusion coefficients on power exhaust*

In the divertor simulation, the radial diffusion coefficients of the SOL plasma are primary key parameters to determine profiles of the heat and particle fluxes. For the recent DEMO simulations, $\lambda_{q//}^{mid}$ of the total (electron and ion) $q_{//}$ profile was within a range of 2 – 3 mm, while different diffusion coefficients were used as shown in Sec. 3.1 and Table 3. The effects of smaller $\lambda_{q//}^{mid}$, which was produced by reducing diffusion coefficients, on the partial detachment and divertor operation were investigated in JA-DEMO [14,15]. Some representative simulations with both χ and D reduced to half values, i.e. $\chi_e = \chi_i = 0.5$ m^{2}s^{-1} and $D = 0.15$ m^{2}s^{-1}, were performed for the four series shown in Sec. 3.2. Profiles of electron, ion and total parallel heat fluxes near the X-point ($q_{//e}^{Xp}$, $q_{//i}^{Xp}$ and $q_{//e}^{Xp} + q_{//i}^{Xp}$) for Case-1 ($P_{sep}$ ~ 235 MW, f^{*div}_{rad} ~ 0.8 and the same n_e^{sep} of 2.0×10^{19} m^{-3}) are compared in Fig. 11 (a) and (c), mapping to the outer midplane radius (r^{mid}). Here, radial gradients of T_e^{Xp}, T_i^{Xp} and n_e^{Xp} profiles were generally increased for the reduced χ and D case, and the increase in T_i^{Xp} (from 820 to 1190 eV for the same n_e^{sep} cases) was significant due to reduction in n_e^{Xp} in the SOL region. Both $q_{//e}^{Xp}$ and $q_{//e}^{Xp} + q_{//i}^{Xp}$ profiles are described approximately by a two-exponential function such as $q_{//}(r^{mid}) = q_{//}^{near} exp(-r^{mid}/\lambda_{q//}^{near}) + q_{//}^{far} exp(-r^{mid}/\lambda_{q//}^{far})$, where $\lambda_{q//}^{near}$ and $\lambda_{q//}^{far}$ are e-folding lengths of "near-SOL" and

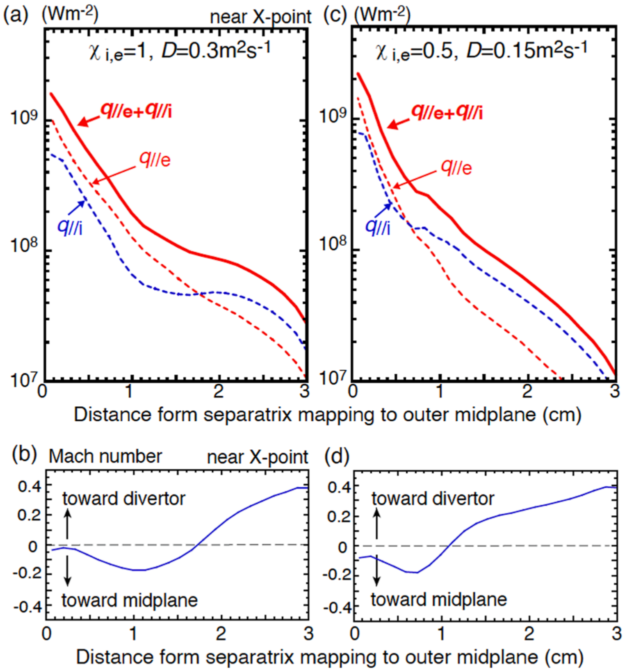

Fig. 11. Electron, ion and total parallel heat flux profiles ($q^{Xp}_{//e}$, $q^{Xp}_{//i}$, $q^{Xp}_{//e} + q^{Xp}_{//i}$) in the Low-Field-Side SOL near the X-point; (a) standard χ and D case (1.0 and 0.3 m^2s^{-1}) and (c) smaller case (0.5 and 0.15 m^2s^{-1}). Mach number profiles of the parallel plasma flow in the SOL near the X-point; (b) and (d), respectively. Minus value corresponds to the plasma flow towards the outer midplane, i.e "flow reversal". Distance from the separatrix near the X-point is mapped to the midplane SOL radius [15].

"far-SOL", and the former is mostly attributed by the electron conductive transport. $\lambda^{near}_{q//}$ values of $q^{Xp}_{//e}$ and $q^{Xp}_{//e} + q^{Xp}_{//i}$ profiles become smaller (from 2.3 to 1.6 mm and from 2.9 to 2.2 mm, respectively) mainly due to reduction of the radial diffusion and enhancement of the parallel conductive transport. Reference [15] (Fig. 6 (e)) showed that $\lambda^{near}_{q//}$ values of four representative $q^{Xp}_{//e} + q^{Xp}_{//i}$ profiles for the different P_{sep} and f^{*div}_{rad} cases were 1.2 – 1.6 times larger than those for the $q^{Xp}_{//e}$ profiles, and they were decreased from 2.5 – 3.3 mm (for the reference χ and D) to 1.7 – 2.2 mm for the reduced χ and D case.

On the other hand, the transition from the "near-SOL" to the "far-SOL" in the $q^{Xp}_{//e} + q^{Xp}_{//i}$ profile is attributed to the $q^{Xp}_{//i}$ profile, i.e. ion transport. Simulation results suggested that "flow reversal" [52] is produced above the outer divertor target by locally increasing neutral ionization and plasma pressure, and that it is extended to the low-field-side SOL. Fig. 11 (b) and (d) show Mach number ($V_{//}/C_s$) profiles of the plasma flow near the X-point, where the flow reversal is seen in $r^{mid} \leq$ 1.7 cm and $\leq$ 1.1 cm, respectively. The parallel convective transport is produced in the same direction. The $q^{Xp}_{//i}$ profile shows the ion heat flux towards the outer divertor, thus the convective heat flux produced by the flow reversal is not included. Flat "shoulder" in the $q^{Xp}_{//i}$ profile becomes more significant as radially extending the convective heat flux by the flow reversal, as shown in Fig. 11 (a). Since contribution of $q^{Xp}_{//i}$ on the $q^{Xp}_{//e} + q^{Xp}_{//i}$ profile becomes larger than $q^{Xp}_{//e}$ at the outer r^{mid}, the transition from the "near-SOL" to the "far-SOL" is seen outward in the $q^{Xp}_{//e} + q^{Xp}_{//i}$ profile for the standard χ and D case. Fig. 11 also shows that the transition locations of (a) $r^{mid} \sim 1.1$ cm and (c) $r^{mid} \sim 0.7$ cm correspond to peaks of the flow reversal profiles. These locations also correspond to flux surfaces of the detach-attach boundary at the outer target ($r^{div} \sim 12$ cm and ~ 7 cm, respectively). At the same time, the peak q_{target} was produced in the attached region, as shown in Reference [14] (Fig. 5), and the peak is increased from 5.8 to 9.5 MWm^{-2} mostly due to increases in the local T^{div}_e and T^{div}_i. Since the "flow reversal" reduces the impurity retention above the divertor target, the radiative cooling may not be efficient at the downstream of the flow reversal peak. These simulation results suggested that the "flow reversal" formation affects the partial detachment profile and the peak q_{target} as well as the parallel heat flux profile in SOL.

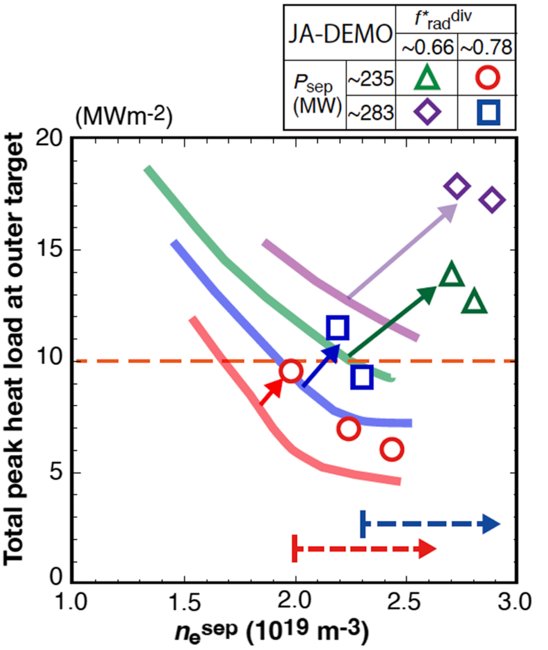

Fig. 12. Representative peak q_{target} at the outer target for four series of P_{sep} ($\sim$235/283 MW) and f^{*div}_{rad} ($\sim$0.67/0.78) as a function of n^{sep}_e [14]. Open symbols show corresponding four results with transport coefficients reduced a factor of two ($\chi_e = \chi_i = 0.5$ m^2s^{-1} and $D = 0.15$ m^2s^{-1}). Four guidelines correspond to results with standard χ and D from Fig. 6.

Results of the peak q_{target} at the outer target for the smaller χ and D cases are added to the results of Fig. 6, with open symbols in Fig. 12. Similar to those in Sec. 3.2, the peaks of q_{target} are increased with increasing P_{sep}·(1-f^{*div}_{rad}) and they are reduced with increasing n^{sep}_e for each case. The lower boundary of n^{sep}_e for $q_{target} \leq 10MWm^{-2}$ is determined to be 2.0×10^{19} and 2.3×10^{19} m^{-3} for the reference f^{*div}_{rad} ($\sim$0.78) cases: $P_{sep} = 235$ MW (red) and 283 MW (blue), respectively. Therefore, the Case-1 is acceptable in the low n^{sep}_e operation, but higher n^{sep}_e ($\geq 2.3\times10^{19}$ m^{-3}) is required for the Case-2. On the other hand, for the lower f^{*div}_{rad} ($\sim$0.67) cases, the peak q_{target} and n^{sep}_e are significantly increased with decreased partial detachment width and increased local T^{div}_e and T^{div}_i. Thus the divertor operation is difficult in the low n^{sep}_e range. As a result, the reduction in χ and D significantly affected the divertor power exhaust due to increase of the $q_{//i}$ profile in the far-SOL as well as the dominant $q_{//e}$ near the separatrix. In order to produce the detached plasma at the significantly large $q_{//}$ region and to reduce the peak $q_{target} \leq 10MWm^{-2}$, high f^{*div}_{rad} of 0.8 level was necessary for the JA-DEMO divertor design.

4. Divertor target and heat removal design

4.1. Design concepts and key design parameters

Conceptual designs of the plasma facing components (PFCs) and coolant routing in the divertor cassette have been developed based on divertor simulation results. Since steady-state power handling of 10 MWm^{-2}-level peak heat load is a common requirement for the conventional divertor design, the water-cooled target of the ITER technology, i.e. W-monoblock (W-MB) and Cu-alloy (CuCrZr) cooling pipe [25], is a primary baseline concept. On the other hand, engineering design adequate for higher neutron irradiation condition is required for the DEMO design. Recent design concepts are summarized in Table 5;

Table 5
Key components and parameters of armor, heat sink and cassette for water-cooling divertor concepts of EU-DEMO, JA-DEMO, CFETR and K-DEMO.

		EU-DEMO [53,54]	JA-DEMO [18]	CFETR [46,55]	K-DEMO [22]
Number of cassette		48	48	80	32 (upper/lower)
Number of divertor maintenance ports		16	16	16	16
Total cassette weight incl. PFC units (ton)		8.3	~ 22	~ 8	TBD
Target	Plasma facing component	W	W	W	W
	Heat sink pipe	CuCrZr	CuCrZr	CuCrZr	CuCrZr/RAFM-steel
	Water temperature (°C)/ P(MPa)	130/ 5	200/ 5	140–180/ 5	70/4 or 290/15
	Dose rate on PFC ($\text{dpa}\cdot\text{FPY}^{-1}$)	< 1.9	< 0.5	< 0.5	< 0.4
	Dose rate on cooling pipe ($\text{dpa}\cdot\text{FPY}^{-1}$)	< 7.2	< 1.5	< 1.5	<1.9 or < 1.2
Upper target (Baffle)	Plasma facing component	(*1)	W	W	W
	Heat sink pipe	—	F82H	CuCrZr/RAFM-steel	RAFM-steel
	Water temperature (°C)/ Pressure (MPa)	—	290/ 15	140–180/ 5	150/ 5
	Dose rate on PFC ($\text{dpa}\cdot\text{FPY}^{-1}$)	—	< 2	< 2	< 2.6
	Dose rate on cooling pipe ($\text{dpa}\cdot\text{FPY}^{-1}$)	—	< 6	< 6	< 10.9
Dome (Liner)	Plasma facing component	W (*1)	W	W	W
	Heat sink pipe	EUROFER97	F82H	CuCrZr/RAFM-steel	RAFM-steel
	Water temperature (°C)/ Pressure (MPa)	180/ 3.5	290/ 15	140–180/ 5	150/ 5
	Dose rate on PFC ($\text{dpa}\cdot\text{FPY}^{-1}$)	< 1.8	< 1.6	< 2	< 1.9
	Dose rate on cooling pipe ($\text{dpa}\cdot\text{FPY}^{-1}$)	< 5	< 5	< 6	< 7.8
Cassette	Structural material	EUROFER97	F82H	SS316L/RAFM-steel	RAFM-steel
	Water temperature (°C)/ Pressure (MPa)	180/ 3.5	290/ 15	140–180/ 5	290/ 15
	Dose rate on structural material ($\text{dpa}\cdot\text{FPY}^{-1}$)	< 6	< 3	TBD	TBD

Note *1) Baffle is not installed. Liner is installed for protection against the plasma and neutron irradiation.

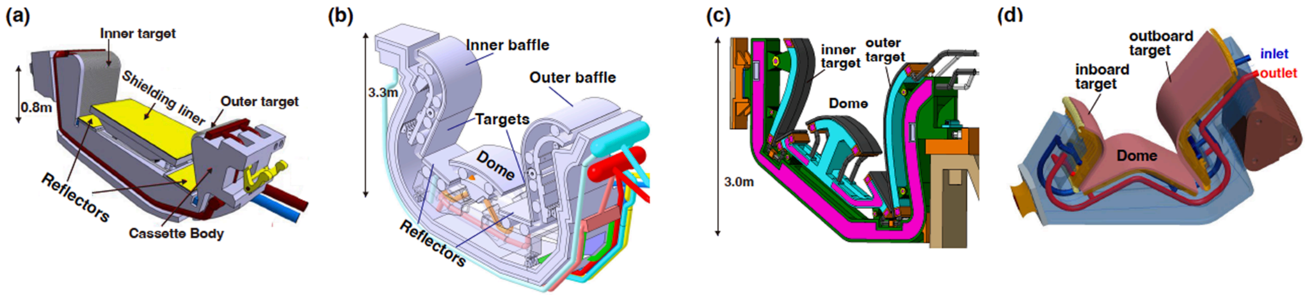

Fig. 13. Recent divertor designs for (a) EU-DEMO [54], (b) JA-DEMO [18], (c) CFETR [55], (d) K-DEMO [22].

designs of the divertor PFC units and cassette body (CB) for EU-DEMO, JA-DEMO, CFETR and K-DEMO are shown in Fig. 13. The water-cooled target concept is selected for the EU-DEMO as a baseline concept [53,54], which can take advantage of the thermal conductivity and the thermohydraulic properties compared to helium gas. All DEMO concepts have the same number (16) of the toroidal field coils (TFCs), which is less than ITER (18), and the maintenance port is located between TFCs. Three adjacent divertor cassettes are replaced through one maintenance port in both EU-DEMO (temporary option) and JA-DEMO. The divertor geometry for EU-DEMO is simplified compared to that of ITER, i.e. baffles are removed, inner and outer target plates cover ~ 0.7 m near the strike-points and a flat shielding liner is installed to protect the vaccum vessel against high neutron irradiation and to prevent gas backflow. The weight of one EU-DEMO divertor cassette is 8.3 tons, which is comparable to that of an ITER divertor cassette. JA-DEMO divertor PFC encloses most of the divertor plasma below the X-point similar to the ITER design, thus the total weight of one cassette (~22 tons) is 2.7 times heavier. In order to reduce each cassette weight for CFETR, the number of the cassettes is increased to 80.

Neutron irradiation doses, i.e. displacement per atom rate (dpa), on the W-MB and the CuCrZr heat sink are significantly increased in DEMO compared to ITER due to increasing operation time as well as the neutron flux. The maximum doses rates for a full-power-year (FPY) operation, i.e. $\text{dpa}\cdot\text{FPY}^{-1}$, become larger than their doses for the full operation period of the ITER divertor, which are expected to produce 0.54 (W-MB) and 2.5 (CuCrZr) [56]. Therefore, the engineering design and technology of the divertor component should consider degradation of material properties and reductions of irradiation damage prior to the scheduled replacement. Table 5 shows that the maximum dose rates on the W-MB and CuCrZr pipe are 1.9 and 7.2 $\text{dpa}\cdot\text{FPY}^{-1}$, respectively, at the upper corner of the EU-DEMO target. The former dose rate on the W-MB is comparable to those at the baffle for the other DEMO divertors, which apply the reduced activation ferritic martensitic (RAFM) steel pipe to the heat sink. It is noted that dose rates on the W-MB and CuCrZr pipe near the outer strike point for EU-DEMO are ~1 and 2 – 3 $\text{dpa}\cdot\text{FPY}^{-1}$, respectively [54], both of which are larger than ~0.4 and ~1.2 $\text{dpa}\cdot\text{FPY}^{-1}$ for JA-DEMO [6], due to the influence of shallow divertor geometry and larger P_{fusion}.

Under severe neutron irradiation condition, reduction in thermal conductivity of the W-MB and coolant pipe, and degradation of their mechanical properties become critical issues to determine the replacement of the water-cooled divertor target in addition to various surface damages and erosion caused by the plasma irradiation as expected in ITER. For the former two factors, design issues of the PFC unit and coolant condition are explained below. Replacement of the W-MB and heat sink is prefered to be done at the same time as that of the breeding blankets (BBs) such as once in 3–4 years, which is determined by the dose restriction (such as 50 dpa) on the structual material (RAFM-steel) and the maximum $\text{dpa}\cdot\text{FPY}^{-1}$ on the BB for EU- and JA-DEMOs [57,58].

Reduction in the thermal conductivity of the W-MB due to the nuclear transmutation to Re and Os reaching 1 – 2 wt% at several dpa [59] will be acceptable at the high surface temperature of 500 – 1200 °C. Further factors to reduce the conductivity and mechanical properties of the armor material, i.e. bulk-W and W-alloy, by neutron irradiation and plasma surface interaction were reviewed in other references [60,61]. As shown in Sec. 3.4, net erosion by the plasma irradiation may become a lifetime issue under the partial detached divertor condition. In addition, recrystallization will progress even at lower temperature for year-long operation such as reducing surface temperature to ~900 °C after 2.4 years [62], where the steady-state peak $q_{\rm target}$ may be reduced less than 10 MWm^{-2} in the later period.

Selection of Cu-alloy (CuCrZr and Cu-base composites) as the heat sink for the high heat load target is owing to their excellent thermal conductivity. On the other hand, replacement of the water-cooled target will be determined firstly by the dose on the heat sink, while the dose on the support structure (RAFM steel) is also important. Constraint factors on the material properties and their appearance doses under the neutron irradiation condition are shown in Table 6 [63]. First, radiation induced hardening at the lower temperature starts from the low irradiation dose (~0.2 dpa), then radiation induced softening and creep are anticipated at high temperarture ($>$ 280 – 300 °C) above 1 – 2 dpa [63,64]. Therefore, degradation of the mechanical property of the Cu-alloy pipe at high temperarture with 1 – 2 dpa is anticipated as a critical lifetime issue for the high heat load PFC in JA-DEMO, K-DEMO and recent CFETR divertors, and these designs consider that it is used only for the target. For the higher dose rate (up to 5 – 6 dpa·FPY^{-1}) but lower heat load (lower than a few MWm^{-2}) region such as the baffles, reflectors and dome, the RAFM-steel pipe is applied to the heat sink. JA-DEMO anticipates replacement of the inner and outer targets after 1 – 2 year long operations, i.e. more frequently compared to the BB replacement. At the same time, the coolant temperature ($T_{\rm cool}$) for the high heat flux component is increased to higher than that of ITER (~70 °C). The selection of $T_{\rm cool}$ has large variation between 70 °C and 200 °C at the conceptual design stage, i.e. K-DEMO: 70 °C, EU-DEMO: 130 °C, CFETR: 140 – 180 °C, JA-DEMO: 200 °C. On the other hand, for the EU-DEMO, it is tentatively assumed that the key mechanical behavior of the CuCrZr heat sink irradiated for two FPYs would not significantly change at least up to 10 dpa (reduction of thermal condictivity by transmuted product), considering the pronounced mechanical saturation behavior of CuCrZr specimens irradiated and tested at low temperature (150 °C) after a low irradiation dose ($\leq$ 0.6 dpa) [65]. Lower $T_{\rm cool}$ (130 °C) for EU-DEMO is determined mainly by the requirement to ensure a safety factor of 1.4 (i.e. 40 % margin) to the critical heat flux (CHF: 45 MWm^{-2}) of the coolant for the slow-transient high heat load of 20 MWm^{-2} with 10 s. Additional discussions of the coolant condition are described in Sec. 4.2.2 and 4.2.3. A comprehensive database of these properties, design criteria and their improvement are required to determine the life time of the power handling unit.

4.2. Design status and issues of heat removal components, cassette and coolant condition

Design of the plasma facing component (PFC) for the 10 MWm^{-2}-level peak heat load, arrangement of coolant routing and selection of the coolant condition have been investigated for the different DEMO divertor concepts. Design status is shortly reviewed, and common design issues are clarified below.

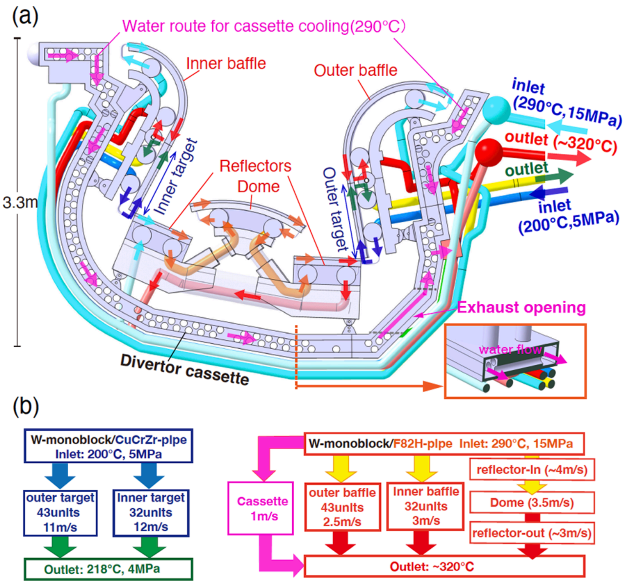

Fig. 14. Design of JA- DEMO divertor (2020): (a) arrangement of the targets, baffles, reflectors, dome and cooling pipes in a cassette, (b) flow velocity (inlet), coolant temperature and pressure in the CuCrZr and F82H pipes for the heat sink units. Here, heat removal is evaluated assuming both the inner and outer $q_{\rm target}$ to be 10 MWm^{-2}, which was larger than the simulation result in Sec. 3.2. [18].

4.2.1. High heat flux PFC and coolant route design

The arrangements of the JA-DEMO divertor and the coolant routes are shown in Fig. 14 (a) and (b). The W-MB and CuCrZr pipe PFC units cover the high heat load region of 0.8 m near the inner and outer strike-points. The coolant route for the two targets is recently revised to be parallel circuit [18] in order to supply the coolant with the velocity ($V_{\rm cool}$) of 14 – 16 m·s^{-1} in the swirled pipe. This reduces the pressure drop to be less than 1 MPa at the inner target incorporating a smaller number of W-MB units, i.e. 32 and 43 for the inner and outer units. In addition, corrosion on the inner wall of the pipe above 200 °C is a common design issue. Corrosion of the inner target pipe by the high $T_{\rm cool}$ and $V_{\rm cool}$ coolant will be reduced.

The divertor configuration and coolant routing for the EU-DEMO have been revised to the one shown in Fig. 15 (a-c) [54]. The length of the vertical target (VT) of ~0.7 m is comparable to the JA-DEMO divertor target (~0.8 m). The parallel circuit concept is also a baseline of the EU-DEMO divertor. The coolant route is divided to the inner and outer targets (incorporating 32 and 44 W-MB units, respectively), and $V_{\rm cool}$ is comparable for both targets (14 – 16 m·s^{-1} in swirled cooling pipe). The parallel circuit design for the high heat flux PFCs becomes a common design for the two DEMO divertors, while the series circuit is used for the ITER divertor.

The W-MB and F82H pipe unit is used in the higher neutron irradiation region of the JA-DEMO divertor such as the dome, reflectors and

Table 6
Design constrains of Cu and Cu-alloy under neutron irradiation condition [63].

	Softening				Embrittlement	Thermal cond.reduction
Heat sink/ Coolant pipe	Yield strength at RT (MPa)	Threshold (℃)	Radiation-induced (dpa)		Embrittlement by transmuted He (dpa)	Reduction (20%) by transmuted product (dpa)
			hardening	softening		
Cu	~ 60 MPa	—	~ 0.1	—	6 (at 350℃) 40 appm limit with 7appm/dpa	10
CuCrZr	> 400 MPa	280	~ 0.2	~ 1		10
ODS-Cu(GlidCop® [63])	> 400 MPa	300	~ 0.2	1 ~ 2		10

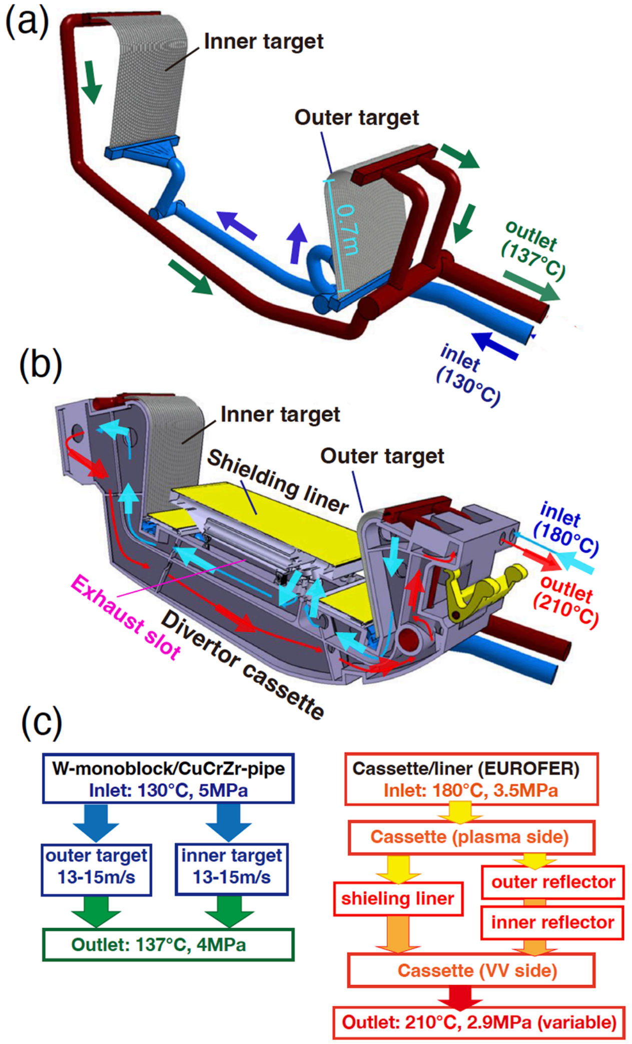

Fig. 15. Recent design of EU-DEMO divertor (2019) [54]: (a) cassette with target plates, shielding liner and cooling manifold with higher temperature (180–210 °C) coolant route shown by arrows. (b) Arrows show lower temperature (130–140 °C) coolant route for inner and outer targets. (c) Flow velocity, coolant temperature, pressure for targets and cassette body.

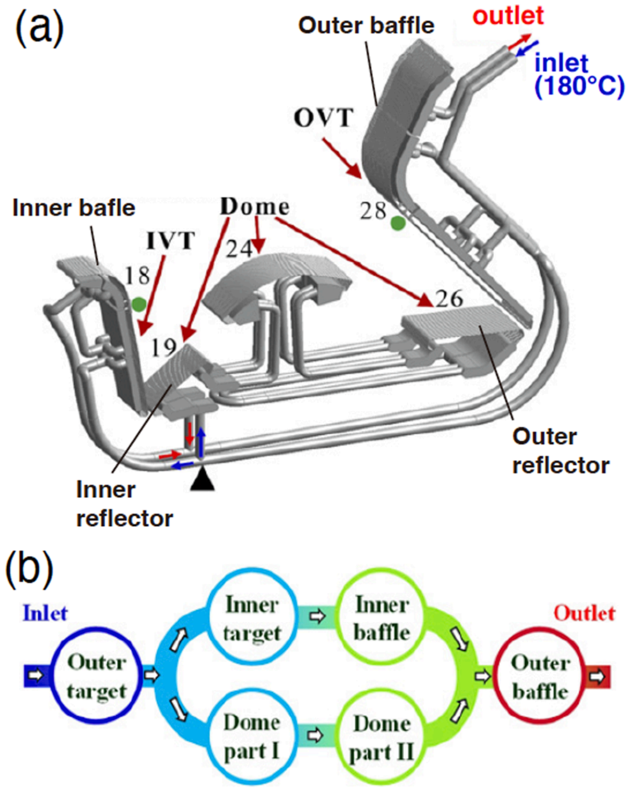

Fig. 16. (a) Hybrid coolant circuit concept for CFETR divertor [55]; OVT: outer target and baffle; IVT: inner target and baffle; Dome: umbrella, inner and outer reflector plates. The number labels show the quantity of the cooling unit channels. (b) Schematic of streaming sequence of the coolant. Dome part I and II describe Dome module divided toroidally.

baffles. Higher T_{cool} and pressurized water (290 °C, 15 MPa) similar to the BB design [67] is used for the electricity generation by turbine system similar to a pressurized water fission reactor (PWR). The maximum heat load to the W-MB surface is 1 – 1.5 MWm^{-2} and V_{cool} is relatively small (3 – 4 $m{\cdot}s^{-1}$) in the steady-state operation. Thus, the coolant route to the dome and reflectors is arranged by a series connection due to reducing the route branches and joints as shown in Fig. 14 (b). On the other hand, it is revised to the parallel one to exhaust the nuclear heat on the support structures as well as the PFC units.

The divertor configuration and water routing for the CFETR were recently improved. The divertor design and coolant routing was developed from a simple parallel one [46] to a hybrid one [55] as shown in Fig. 13 (c) and 16 (a), respectively. The divertor consists of three plasma facing modules (inner target, dome and outer target) and the CB, and all components are cooled by single coolant condition. The former design proposed that reflector plates and baffle were connected to the target module, where the CuCrZr pipe is used for all target and dome modules. Low T_{cool} (140 °C, 5 MPa) coolant was provided in parallel to inlets of the three modules in order to provide similar flow velocity of 10 $m{\cdot}s^{-1}$ to the inner and outer targets since the in-out asymmetry of the W-MB unit numbers (18 and 28, respectively) is larger than those for EU- and JA-DEMO divertors. A hybrid routing is proposed to improve the heat removal of the outer target more efficiently, and to apply the W-MB units with RAFM-steel pipes at baffles and dome similar to the JA-DEMO divertor. Therefore, T_{cool} is increased to 180 °C comparable to the CB coolant for the EU-DEMO divertor. The flow scheme is shown in Fig. 16 (b). In the hybrid circuit, the main coolant flow is provided to the inner vertical target (IVT), then divided to the inner target and baffle route and to the dome one in parallel. The two routes are merged into the outer baffle. Here, the dome circuit is separated toroidally to two half structures (Dome part I and II), and the coolant circulates through the inner reflector, dome and outer reflector of the Dome part I, then it is returned in the Dome part II. The mass flow rates for IVT and Dome routes are 12.2 and 7.1 $kg{\cdot}s^{-1}$, respectively. The pressure drop for the two routes is similar (0.79 MPa), but the total one from the OVT to the outer baffle is increased to 1.95 MPa.

Finally, the K-DEMO divertor consists of simply three plasma facing modules (inner target, dome and outer target) and the CB as shown in Fig. 13 (d) [22]. The dome structure is low height and extends to the inner and outer reflectors. While the coolant routing is not proposed, thermal analysis on the W-MB units with CuCrZr and RAFM-steel pipes is performed under the steady-state peak heat load of 10 MWm^{-2} [68]. The W-MB size with the CuCrZr pipe is comparable to that of ITER and that with RAFM-steel pipe is smaller, and the coolant conditions correspond to 70 °C/4 MPa and 290 °C/15 MPa, respectively. The former shows a similar result to the ITER divertor target, i.e. the maximum temperatures of the W-MB and CuCrZr pipe are ~ 1242 °C and ~ 271 °C, respectively. On the other hand, for the latter case, the maximum temperature reaches a softening boundary of the RAFM-steel (~550 °C) at the pipe top surface even though the pipe thickness is very thin (0.25 mm). Design of the W-MB units and coolant routing is in progress.

4.2.2. Coolant and Cu-alloy pipe temperatures for high heat flux PFC

For the JA-DEMO divertor design, the total thermal power to the PFC surface is assumed to be 325 MW, which includes about 40 % margin above the simulation result (P_{sep} ~ 235 MW), and the total volumetric nuclear heating in the PFCs and the cassette body by neutron and γ-ray fluxes (114 MW) is considered [18]. Total thermal power to the inner and outer target components is dominant compared to the nuclear heat, and the thermal powers to the dome, baffles and reflectors are still larger by the factor of 1.5 – 3. Temperature distribution on the fish-scale surface W-MB and CuCrZr pipe are evaluated under high plasma heat load (peak q_{target} of ~10 MWm^{-2}) and nuclear heating conditions. Since relatively high T_{cool} (200 °C) coolant is provided in order to minimize the irradiation embrittlement, the maximum temperatures of W-MB and CuCrZr pipe correspond to, respectively, ~1190 °C (W-MB), which is just below the critical temperature of W-recrystallization (~1200 °C), and ~350 °C (CuCrZr pipe), where the influence of thermal softening is somehow accommodated above ~300 °C [66].

For the EU-DEMO divertor design, the total thermal power to the PFC surface (targets, shielding liner and reflection plates) is given to be 200 MW, which is 33% above the simulation value of P_{sep} ~ 150 MW, and the total volumetric nuclear heat in the PFC units and the CB is 139 MW [54]. The total thermal power is smaller than that of the JA-DEMO divertor design due to smaller P_{sep} and design margin, and the nuclear heat is larger due to larger P_{fusion}. For the local coolant temperature of 150 °C near the strike point, the maximum temperatures of the CuCrZr pipe are evaluated to be ~310 °C and ~440 °C at the upper location near the strike point for the peak q_{target} of 10 and 20 MWm^{-2}-level, respectively, corresponding to the steady-state and slow transient cases. The former is slightly higher than the optimal temperature range of 250 – 300 °C, and the latter is expected to cause a reduction in the yield strength, in particular, under the neutron irradiation. Inlet T_{cool} is recently reduced from 150 to 130 °C in order to increase the CHF to larger than 45 MWm^{-2} as shown in Table 5.

As a result, the lower T_{cool} design is preferable from the viewpoints of the influence of thermal softening even for the maximum steady-state heat load (~10 MWm^{-2}) for the DEMO divertor design. On the other hand, T_{cool} (130 °C) is lower from the viewpoint of the thermal recovery temperature (150 – 200 °C) of irradiated CuCrZr pipe. A comprehensive material database of Cu-alloy in T_{cool} (130 – 200 °C) range will be demanded for the divertor operation and determination of the replacement.

4.2.3. Thermal stress evaluation on high heat flux PFC

Elasto-plastic analysis with repeating high heat load is a common method to evaluate strain from the initial shape and thermal stress on the PFC component, which was performed for the JA-DEMO divertor target under the high peak q_{target} (10 and 15 MWm^{-2}) plus the nuclear heating condition [18], while non-irradiation stress–strain database was used. The maximum heat fluxes of 18 and 22 MWm^{-2}, respectively, are widely distributed on the water side of the CuCrZr pipe, which corresponded to 64% and 79% of CHF (28 MW m^{-2}) of the high T_{cool} (200 °C) coolant. For the latter case, the maximum temperature of the CuCrZr pipe was increased to ~380 °C. Expansions in the pipe axis (z) and circumferential (θ) directions are seen in the CuCrZr pipe under the MB tile, and compression is caused between MB tiles. While the stress (σ_Z) – strain (ε_Z) trace at the maximum stress location shows similar trajectory ($\Delta\sigma_Z$ ~ 300 MPa and $\Delta\varepsilon_Z$ ~ 0.25%) with repeated high heat load cycles. Mechanical toughness of the pipe against thermal softening may not be a critical lifetime issue at least for early stage of irradiated condition and the peak q_{target} of 15 MWm^{-2}, but it is anticipated to be critical with increasing the irradiation dose.

Uncertainty and/or limitations in lifetime projections of the CuCrZr pipe and Cu interlayer have been examined for the EU-DEMO divertor. Elasto-plastic analysis of the PFC component investigated under repeated high heat load of 20 MWm^{-2} level by using available neutron irradiation stress–strain database [69,70]. Even under non-irradiation condition, uncertainties come from (i) influences of initial residual stress on the cooling pipe and interlayer, (ii) shakedown response of the elasto-plastic structure in the early cycles, and (iii) loss of its initial yield strength by ageing (softening by thermal ageing) under the long-term cycles (in particular, exceeding the allowable service temperature limit of ~350 °C). For the neutron irradiation cases, the low T_{cool} (130 °C) would be still acceptable (suggested from ITER SDC-IC data) that the total elongation remained > 5% in embrittled CuCrZr pipe (for 0.3 – 5 dpa). Also it could be rather beneficial since the fracture toughness of the pipe (for 0.3 – 1 dpa) with a sub-mm level crack located at the inner wall is decreased with increasing temperature until no margin at ~350 °C for a large crack case. Furthermore, elasto-plastic analysis results suggest that the most likely failure behavior would be accumulated cyclic strain on the CuCrZr pipe surface, in particular, in the gap between adjacent W-MBs, leading to early fatigue cracks and potential coolant leaks. Consequently, elasto-plastic analysis study of the PFC unit (in particular, CuCrZr pipe) under the EU-DEMO divertor operation condition, i.e. the low T_{cool} and slow transient heat load of 20 MWm^{-2} level, has been developed under the above irradiation condition. Evaluation of the lifetime projection is in progress.

Copper interlayer could be hardened and embrittled when transmutation gas bubbles (e.g. helium) are segregated at grain boundaries at higher dose (~6 dpa). Embrittlement of the Cu interlayer leads to substantially high stresses (tensile stress on the W-MB), which may cause a crack formation of the W-MB at or near the bond interface, leading to a local reduction of heat conduction. Distinct consequences of limited knowledge on the actual state of materials and effective loading history are discussed in the light of expected failure modes. Degradation of the mechanical property of the heat sink and joint/interlayer caused by radiation induced softening and/or hardening at the lower dpa can be minimized by application of new W and Cu/Cu-alloy target concepts as shown in Sec. 4.3.

4.2.4. Cassette body and coolant design for DEMO divertors

CB design has been developed for each DEMO divertor to incorporate the power exhaust units and coolant pipes, which should be consistent with reducing the fast neutron flux to protect the vacuum vessel (less than 2.75 dpa for both JA- and EU-DEMO divertors) and replacement of the PFC units [18]. The number of main coolant pipes is minimized to four, and the inlet and outlet are located at the outboard cassette. The cassette structures and coolant conditions are different, but the CB can be made by welding similar RAFM-steel (F82H and Eurofer97).

The JA divertor CB consists of thick (25 cm) plate structures with two lines of cylindrical coolant puddles in order to reduce the fast neutron and γ-ray flux as shown in Fig. 14 (a). The exhaust slot is located at the outboard bottom in order to reduce the neutron flux to the vacuum vessel. The PWR condition coolant (290 °C, 15 MPa) is provided from the inboard and outboard manifolds through the side routes of the CB to the puddles, and it finally exits to a manifold near the exhaust slot. The coolant velocity of 1.5 $m{\cdot}s^{-1}$ is enough to remove the total nuclear heat of 0.7 MW in one cassette body, corresponding to a total of 32 MW for 48 cassettes.

The EU divertor CB is composed of a box structure with internal ribs, and it is cooled by higher inlet T_{cool} (180 °C, 3.5 MPa) coolant as shown in Fig. 15 (b) and (c), which ensures the entire structure sufficient fracture toughness at the neutron damage (less than 6 dpa) [54]. The coolant is also used for the liner and reflectors by a series connection. Since the exhaust opening is designed to be at the bottom of the CB, the liner mainly has a role in reducing fast neutron flux to the bottom area of the vacuum vessel. Total nuclear heat for 48 cassettes is 85 MW, which also includes the liner, reflectors and support structures of the target PFC units. In addition, that of 37 MW for the coolant fluid will be considered to evaluate T_{cool} in the circulation route.

The reduction in T_{cool} for the CB and RAFM heat sink of the PFC units is also a trade-off issue between irradiation embrittlement of the RAFM-steel and heat exhaust design. The low T_{cool} for the EU DEMO is determined by the temperature margin (up to 550 °C) of key components such as supports of the reflector and liner plates due to inefficient exhaust of local nuclear heat. For the JA-DEMO divertor CB, local temperatures at the support structures of the inner and outer baffles are higher than 600 °C. Improvement of the heat exhaust design and the T_{cool} optimization are required.

4.3. Development of divertor target technologies for DEMO

The mechanical properties of the heat sink, the thermal contact to interlayer and the W-MB are important key issues for Cu-alloy application under neutron irradiation. Several technologies for the high heat flux target have been developed in the EU to survive under DEMO-relevant neutron irradiation conditions. All are based on W-MB as a baseline plasma facing material, and Cu-alloy pipe with swirl tape to increase the heat transfer at the pipe wall [71,72]. Material properties of CuCrZr and Cu-interlayer are anticipated to limit the performance of the target heat sink, e.g. irradiation creep above 350 °C and irradiation embrittlement below 250 °C [66]. Thus, the pipe is reinforced by various kinds of Cu-W composite materials and novel interlayer materials as shown in Fig. 17 [54].

(a) The ITER-like W-MB with a CuCrZr pipe [71,73] is a baseline concept also in the DEMO divertor, but the MB size is modified to decrease the cross-section width to 23 mm, instead of 28 mm in ITER in order to reduce thermal stresses and prevent vertical cracking. The axial block thickness of 12 mm and front face armor thickness of 8 mm above the cooling pipe are the baseline design.

(b) The thermal break interlayer concept (developed in Culham Centre for Fusion Energy: CCFE) is based on the ITER W-MB target [74]. The concept features cut-outs in the Cu-interlayer in the area of the highest heat flux to achieve a more uniform distribution of the thermal flux around the cooling pipe circumference.

(c) The composite pipe concept (developed in Max Planck Institute for Plasma Physics: IPP Garching) is based on a W wire-reinforced Cu composite pipe [75], which expects better strength of the cooling pipe, in particular, at high temperature (>350 °C).

(d) The functionally graded W/Cu (FGM) interlayer concept (developed in the French Alternative Energies and Atomic Energy Commission: CEA) aims to replace the thick Cu interlayer [76], which is expected to be fully embrittled by fast neutron due to segregation of transmuted He at grain boundaries. Graded thin (20 μm) and thick (500 μm) W-Cu interlayer is used to improve joining strength.

(e) The flat-tile concept with a composite heat sink block (developed in Max Planck Institute for Plasma Physics: IPP Garching) uses W-particle-reinforced Cu composite block [77,78] and it is expected to enhance the mechanical resilience of the irradiated heat sink against structure failure. The use of the W-Cu composite is supposed to reduce the thermal expansion mismatch between the armor tile and the heat sink block.

(f) In addition, He cooling of the target using multi-jet pipe by W and W-laminate (developed in Karlsruhe Institute of Technology: KIT) is also developed as a long-term option [71].

Recently, small-scale mock-ups of each concept have been fabricated and tested by means of hydrogen neutral beam in the GLADIS irradiation facility in IPP Garching under the high power density at 20 MWm^{-2} up to 2000 cycles (130 °C coolant, which is the expected operation temperature). A good production quality and reliable high-heat-flux fatigue performance was demonstrated. All mock-ups showed intact structural integrity and stable heat removal capacity over the entire loading cycles. Modest roughening of the W-MB surface and swelling of the blocks due to inelastic deformation was found. The metallographic examination revealed that the upper half of the MBs were completely recrystallized, but no discernable cracks were found in any of the tested armor (290 blocks). Furthermore, other ITER-like mock-ups were tested at 25 MWm^{-2} up to 1000 pulses (20 °C and 105 °C coolant conditions) for overload tests [79]. Also under the increased heat load, the mock-ups exhibited intact structural integrity and stable heat removal capacity, even though there was a single fine crack (6 mm in depth) initiated from the MB surface which underwent a pronounced inelastic deformation leading to overall severe roughening. The mock-ups even withstood the overload up to 32 MWm^{-2} (5 pulses), which was the physical limit nearly reaching the melting temperature of the W-MB surface without any detrimental impact nor melting. The future R&D will be focused on an upscaling trial towards a medium-scale manufacturing prototype (40 cm length).

Since oxide dispersion strengthened copper alloy (ODS-Cu) is also a suitable heat sink under the higher temperature and neutron irradiation condition as shown in Table 6, an advanced brazing technique (ABT) has been developed in Japan (National Institute for Fusion Science: NIFS) to join oxide dispersion strengthened copper alloy (ODS-Cu, i.e. such as Cu-0.3 wt%Al2O3: GlidCop®) heat sink and W-armor tile with the BNi-6 (Ni-11%P) filler material [80]. Recently, advanced multi-step brazing (AMSB) technique was applied to join ODS-Cu, W, and SUS with ODS-Cu

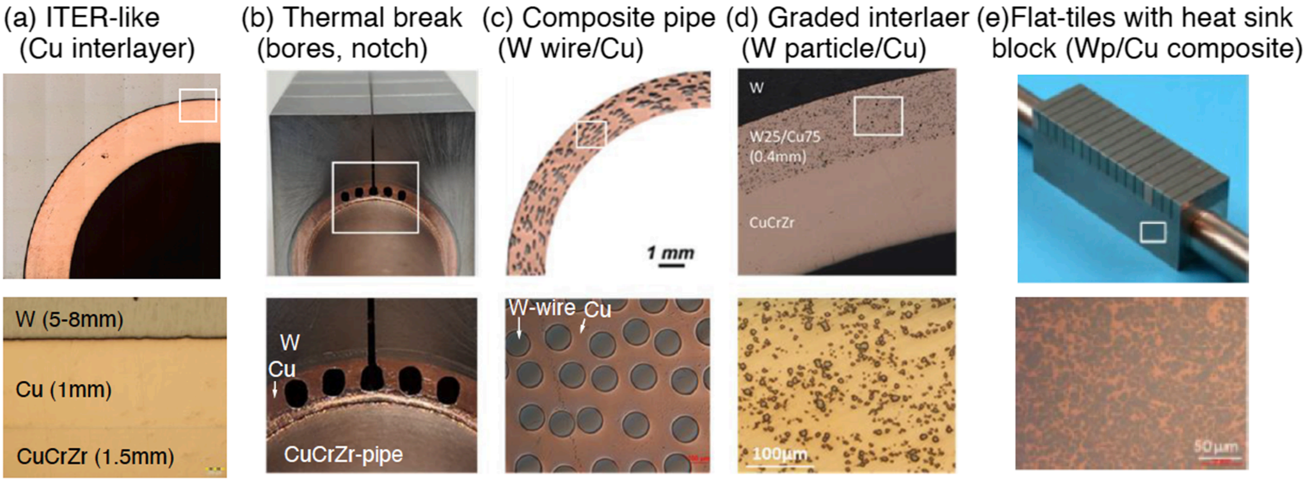

Fig. 17. High heat flux target technologies developed for EU-DEMO divertor [54]: (a) ITER-like monoblock baseline concept, (b) thermal break interlayer concept, (c) composite pipe of W-wire in Cu (Wf/Cu), (d) graded interlayer, (e) Flat W-tiles and W particle/Cu composite block. Bottom row of images show close up of region inside white rectangle above.

[81], so that prototype components for the divertor heat removal unit were successfully fabricated [63,82]. The component has a rectangle-shaped coolant flow path with V-shaped staggered rib (fin) structures in the flow path. High heat load tests by the electron beam device (ACT2 in NIFS) showed excellent heat removal capability up to 30 MWm^{-2} (15 °C, ~0.5 MPa water condition), using some heat removal enhancement such as turbulent flow and fine-scale local nucleate boiling. Optimization of the flat W-tile component and application to W-MB unit are planned for the future R&D.

5. Summary and future issues

The power exhaust concept and appropriate divertor design are common critical issues for DEMO design activities, which have been carried out in Europe, Japan, China, Korea and the USA. At the same time, the divertor design is strongly affected by DEMO missions (net electricity generation, sufficient tritium breeding and feasibility for remote maintenance) and the design requirements from each DEMO concept. In this paper, conventional divertor concepts and steady-state power exhaust studies for recent representative DEMO designs (P_{fusion} = 1 – 2 GW, R_{p} = 7 – 9 m) were reviewed from the viewpoints of the plasma physics issures and the engineering design. Radiative cooling is a common approach for the power exhaust scenario, and water-cooled divertor design with ITER-like target (W-PFC and Cu-alloy heat sink) is a common baseline. Common views and differences in the divertor designs are summarized below, and critical issues and challenges are clarified. Some different design approaches have provided important case-studies of the DEMO divertor, and those will contribute to future improvements and developments of the DEMO divertor design.

(1). Requirements of plasma performance and constraints on $f_{\mathrm{rad}}^{\mathrm{main}}$ determine the divertor design concept:

Different power exhaust scenarios have been developed for DEMO concepts, while a common critical issue is the large power exhaust required to accomodate for P_{heat} = 280 – 600 MW. This demmands strong mitigation in the main plasma and divertor by the radiative cooling ($P_{\mathrm{rad}}^{\mathrm{tot}}/P_{\mathrm{heat}} \geq 0.8$). The steady-state plasma concepts such as in JA-DEMO and CFETR proposed a conventional closed divertor geometry to challenge even large $P_{\mathrm{sep}}/R_{\mathrm{p}}$ handling (25 – 30 MWm^{-1}) in order to maintain the ITER-level radiation fraction of the main plasma ($f_{\mathrm{rad}}^{\mathrm{main}} = P_{\mathrm{rad}}^{\mathrm{main}}/P_{\mathrm{heat}} = 0.3 – 0.4$) and higher plasma performance (HH_{98y2} = 1.2 – 1.4). K-DEMO and FNSF will challenge larger $P_{\mathrm{sep}}/R_{\mathrm{p}}$ handling (37 – 53 MWm^{-1}) with the double-null divertor configuration. The repeating long pulsed plasma concept (EU-DEMO) challenges both increasing $f_{\mathrm{rad}}^{\mathrm{main}}$ to ~0.65 with the ITER-level plasma performance (HH_{98y2} = 1.0 – 1.1) and handling the ITER-level $P_{\mathrm{sep}}/R_{\mathrm{p}}$ in an open divertor geometry. The reactor plasma parameters B_{T} and R_{p} as well as exhaust power (P_{sep}) for the EU-DEMO were rather restricted by requirements of the divertor design for handling transient heat load due to divertor re-attachment, excessive impurity concentration to achieve the divertor detachment, and P_{sep} larger than $P_{\mathrm{LH.}}$ Optimization of competing requirements, i.e. increasing $f_{\mathrm{rad}}^{\mathrm{main}}$ vs. the plasma performance ($HH_{98(y,2)}$, β_N, f_{BS}), is a common critical issue for these design concepts, and future experimental and modelling database will improve the power handling requirement for the divertor.

In addition, adequate performance of the power exhaust will be required in relatively low density plasmas. Design improvement is required from the viewpoints of reduction in the fuel dilution, and the power exhaust in the main plasma and divertor.

(2). Power exhaust simulations for DEMO divertor design (P_{sep} = 150 – 300 MW) are in progress and key issues for the plasma modelling of the partial detachment are recognized:

ITER-based divertor geometry (inclined target, baffle and dome structures) with longer leg length (1.6 – 1.7 m) is a common baseline design, and power exhaust simulations for DEMO divertor design with larger P_{sep} = 150 – 300 MW have been performed using integrated divertor codes; SOLPS-ITER on EU-DEMO and CFETR divertors, SONIC on JA-DEMO divertor, UEDGE on FNSF and K-DEMO divertors. Divertor operation and influences of the key power exhaust parameters have been recently investigated with mainly Ar seeding, and all simulations showed reduction in the peak $q_{\mathrm{target}} \leq 10\mathrm{MWm}^{-2}$ for the divertor radiation fraction ($f^{*\mathrm{div}}_{\mathrm{rad}} = (P^{\mathrm{div}}_{\mathrm{rad}} + P^{\mathrm{div}}_{\mathrm{rad}})/P_{\mathrm{sep}}$) of 0.7 – 0.8. Some results were consistent with the design requirement for the $n_{\mathrm{e}}^{\mathrm{sep}}$ range (JA-DEMO: 2 – 3×10^{19}, EU-DEMO: ~3×10^{19} m^{-3}), which were relatively lower than that of ITER. All results also showed that partial detachment was expected in the outer divertor for the vertical target geometry, and the benefit of the closed geometry to reduce the peak q_{target} and $T_{\mathrm{e}}^{\mathrm{div}}$ near the separatrix. A commonly recognized critical issue for the detachment simulations is that the peak q_{target} location and value (and each heat load components) significantly changed in the attached or detached region. In addition, uncertainty of relatively high $T_{\mathrm{e}}^{\mathrm{div}}$ and $T_{\mathrm{i}}^{\mathrm{div}}$ in the attached region (far-SOL) was another critical issue for plasma/impurity transport and tungsten (W) erosion. Further improvements of the divertor geometry and operation options such as different or mixed seeding impurities will be explored to extend the detachment radial width on the target and to reduce local T_e^{div} and T_i^{div} in the attached plasma region.

Radial diffusion coefficients of heat and particle fluxes (χ and D) are critical parameters for DEMO divertor design and operation. Different values and/or profiles were so far applied to produce $\lambda_{\mathrm{q}//}$ =2 – 3 mm near the separatrix in the SOL, which was slightly smaller than that of ITER due to high T_{e} and T_{i} under the SOL condition of tokamak DEMO. Reduction in the assumed χ and D significantly affected the divertor power exhaust due to increase of the $q_{//\mathrm{i}}$ profile in the SOL while the $q_{//\mathrm{e}}$ profile was peaked near the separatrix. The transition location of near-SOL and far-SOL in the heat flux ($q_{//\mathrm{e}} + q_{//\mathrm{i}}$) profile approached to the separatrix. The transition location also corresponded to the flux surface of the detach-attach boundary at the outer target, and the peak q_{target} was increased with reducing the width of the partial detachment. Feasible values or profiles of the diffusion coefficients over the near- and far-SOLs will be required in order to determine the divertor operation for the DEMO design.

SOLPS-ITER simulation results with various drifts activated showed that, for these designs with ion ∇B drift towards the divertor, inboard-enhanced asymmetry of the particle flux profile and outboard-enhanced heat load profile were produced even in the long-leg divertors of EU-DEMO and CFETR. The latter recently proposed to further extend the divertor leg in order to insure the detached divertor operation window at lower $n_{\mathrm{e}}^{\mathrm{sep}}$. Other physics factors that could modify the DEMO divertor design such as enhanced power dissipations in the high density divertor (charge exchange, photon absorption and collisional-radiative models) and kinetic effects in the low collisionality SOL (flux limiter, thermal force) were also pointed out. It is an important common issue to clarify effects of these physics factors for the DEMO divertor conceptual design.

(3). The common baseline design for DEMO divertor and specific design were reviewed, and R&D issues were identified:

Integrated designs of the water cooled divertor target, cassette and coolant pipe routing have been developed, based on the ITER W monoblock (MB) concept with Cu-alloy pipe. Engineering design compatible with the higher DEMO-level neutron irradiation environment is required. Selection and arrangement of the divertor plasma facing unit, coolant condition and routing for recent design concepts of EU-DEMO, JA-DEMO, CFETR and K-DEMO were summarized. Under a year-long DEMO-level neutron irradiation condition, the mechanical properties of the CuCrZr heat sink and the Cu interlayer were anticipated to be embrittled, thus the coolant temperature (T_{cool}) for the high heat flux component was increased to higher than that of ITER (~70 °C). The inlet-T_{cool} selected so far showed a large variation between 70 °C and 200 °C (K-DEMO: 70 °C, EU-DEMO: 130 °C, CFETR: 140 – 180 °C, JA-DEMO: 200 °C). At the same time, the influence of thermal softening on the CuCrZr pipe was evolved near the strike-point when the high heat load of 10 MWm^{-2}-level was applied, in particular, for the higher T_{cool} cases. DEMO specific risks such as neutron induced embrittlement/softening of the interlayers and cooling pipe have been recognized and further restrictions of q_{target} and surface temperature were anticipated. Elast-plastic analysis of the PFC unit under the EU-DEMO divertor operation condition, i.e. lower T_{cool} and slow transient heat load of 20 MWm^{-2} level, has been developed by using available irradiation database. Evaluation of the lifetime projection is in progress. Improved technologies of high heat flux components based on the ITER W-MB unit have been developed in the EU to reduce thermal stress and to strengthen the heat sink and interlayer under higher irradiation dose conditions.

Recent integrated design of the divertor target, CB and coolant pipe routing were also reviewed briefly. Two coolant conditions (low- and high-T_{cool}) were used for the Cu-alloy and RAFM-steel heat sink MB units, respectively, where the latter coolant was also used for the CB and supporting structures. Appropriate conditions for the latter coolant, i.e. 180 – 200 °C/ 5 MPa (EU-DEMO) and 290 °C/15 MPa (JA-DEMO, CFETR and K-DEMO), will be finalized in future optimizations of the divertor and DEMO design concept. Consequently, two coolant conditions and optimization of their circuits will be necessary for the water cooled DEMO divertor. The circuit design also should be appropriate for the remote maintenance and PFC replacement in the hot cell facility. In addition, a common issue of series or parallel cooling circuit routing for the DEMO divertor design was compared. The parallel circuit design for the target high heat flux PFCs becomes a common design for the EU- and JA-DEMO divertors in order to provide similar flow velocity of 10 $\mathrm{m \cdot s^{-1}}$ to the inner and outer targets, while the series circuit is used for the ITER divertor.

CRediT authorship contribution statement

N. Asakura: Conceptualization, Methodology, Formal analysis, Investigation, Writing – original draft. **K. Hoshino:** Software, Methodology, Validation, Writing – review & editing. **S. Kakudate:** Investigation. **F. Subba:** Data curation, Validation, Writing – review & editing. **J.-H. You:** Data curation, Validation, Writing – review & editing. **S. Wiesen:** Validation. **T.D. Rognlien:** Data curation, Validation, Writing – review & editing. **R. Ding:** Data curation, Validation. **S. Kwon:** Data curation, Validation, Writing – review & editing.

Declaration of Competing Interest

The authors declare that they have no known competing financial interests or personal relationships that could have appeared to influence the work reported in this paper.

Data availability

Data will be made available on request.

Acknowledgments

The authors thank Y. Homma (QST), H. Utoh (QST), Y. Somaya (QST), S. Yamoto (QST), Y. Sakamoto （QST）, M. Tokitani (NIFS), Joint Special Design Team for Fusion DEMO (Japan), M. Siccinio (IPP, Garching), G. Mazzone (ENEA), D. Marzullo (Univ. Trieste), S. Roccella (ENEA), H. Greuner (MPG), C. Kessel (ORNL), S.-H. Hong (GA) for giving detailed information and comments. The first author also thanks the continuous support by the Japan and Europe home teams (QST in Rokkasho, and EUROfusion Programme Management Unit in Garching), and DEMO Design Activity (DDA) unit of the IFERC project team.

The SONIC simulations were carried out within the framework of the Broader Approach DEMO Design Activity, using the JFRS-1 supercomputer system at CSC, IFERC, Rokkasho, Japan.

References

[1] R. Wenninger, et al., The physics and technology basis entering European system code studies for DEMO, Nucl. Fusion 57 (2017), 016011.
[2] G. Federici, C. Bachmann, L. Barucca, W. Biel, L. Boccaccini, R. Brown, C. Bustreo, S. Ciattaglia, F. Cismondi, M. Coleman, V. Corato, C. Day, E. Diegele, U. Fischer, T. Franke, C. Gliss, A. Ibarra, R. Kembleton, A. Loving, F. Maviglia, B. Meszaros, G. Pintsuk, N. Taylor, M.Q. Tran, C. Vorpahl, R. Wenninger, J.H. You, DEMO design activity in Europe: progress and updates, Fusion Eng. Des. 136 (2018) 729–741.
[3] G. Federici, et al., Overview of the DEMO staged design approach in Europe, Nucl. Fusion 59 (2019), 066013.
[4] Y. Sakamoto, et al., DEMO Concept Development and Assessment of Relevant Technologies, 25th IAEA Int. Conf. on Fusion Energy (St. Petersburg, Russia, 2014) FIP/3-2Rb.
[5] K. Tobita, et al., Design strategy and recent design activity on Japan's DEMO, Fusion Sci. Technol. 72 (2017) 537.
[6] N. Asakura, et al., Studies of power exhaust and divertor design for a 1.5 GW-level fusion power DEMO, Nucl. Fusion 57 (2017), 126050.
[7] G. Zhuang, G.Q. Li, J. Li, Y.X. Wan, Y. Liu, X.L. Wang, Y.T. Song, V. Chan, Q. W. Yang, B.N. Wan, X.R. Duan, P. Fu, B.J. Xiao, Progress of the CFETR design, Nucl. Fusion 59 (11) (2019) 112010.
[8] K. Kim, et al., Design of K-DEMO for near-term implementation, Nucl. Fusion 55 (2015), 053027.
[9] J.S. Kang, et al., Development of a systematic, self-consistent algorithm for the K-DEMO steady-state operation scenario, Nucl. Fusion 57 (2017), 126034.
[10] C.E. Kessel, D.B. Batchelor, P.T. Bonoli, M.E. Rensink, T.D. Rognlien, P. Snyder, G. M. Wallace, S.J. Wukitch, Core plasma physics basis and its impacts on the FNSF, Fusion Eng. Des. 135 (2018) 356–369.
[11] C.E. Kessel, et al., The ARIES advanced and conservative tokamak power plant study, Fusion Sci. Technol. 67 (2015) 1.
[12] M. Shimada, D.J. Campbell, V. Mukhovatov, M. Fujiwara, N. Kirneva, K. Lackner, M. Nagami, V.D. Pustovitov, N. Uckan, J. Wesley, N. Asakura, A.E. Costley, A.J. H. Donné, E.J. Doyle, A. Fasoli, C. Gormezano, Y. Gribov, O. Gruber, T.C. Hender, W. Houlberg, S. Ide, Y. Kamada, A. Leonard, B. Lipschultz, A. Loarte, K. Miyamoto, V. Mukhovatov, T.H. Osborne, A. Polevoi, A.C.C. Sips, Chapter 1: overview and summary, Nucl. Fusion 47 (6) (2007) S1–S17.
[13] A. Loarte, B. Lipschultz, A.S. Kukushkin, G.F. Matthews, P.C. Stangeby, N. Asakura, G.F. Counsell, G. Federici, A. Kallenbach, K. Krieger, A. Mahdavi, V. Philipps, D. Reiter, J. Roth, J. Strachan, D. Whyte, R. Doerner, T. Eich, W. Fundamenski, A. Herrmann, M. Fenstermacher, P. Ghendrih, M. Groth, A. Kirschner, S. Konoshima, B. LaBombard, P. Lang, A.W. Leonard, P. Monier-Garbet, R. Neu, H. Pacher, B. Pegourie, R.A. Pitts, S. Takamura, J. Terry, E. Tsitrone, T.-O. Group, Chapter 4: power and particle control, Nucl. Fusion 47 (6) (2007) S203–S263.
[14] N. Asakura, et al., Simulation studies of divertor detachment and critical power exhaust parameters for Japanese DEMO design, Nucl. Meter. Energy 26 (2021), 100864.
[15] N. Asakura, et al., Development and application of SONIC divertor simulation code to power exhaust design of Japanese DEMO divertor, Processes 10 (2022) 872.
[16] F. Subba, et al., Modelling of mitigation of the power divertor loading for the EU DEMO through Ar injection, Plasma Phys. Control. Fusion 60 (2018), 035013.
[17] F. Subba, et al., SOLPS-ITER modeling of divertor scenarios for EU-DEMO, Nucl. Fusion 61 (2021), 106013.
[18] N. Asakura, et al., Power exhaust concepts and divertor designs for japanese and european DEMO fusion reactors, Nucl. Fusion 61 (2021), 126057.
[19] L. Aho-Mantila, et al., Predictions of radiation pattern and in–out asymmetries in the DEMO scrape-off layer using fluid neutrals, Nucl. Fusion 62 (2022), 056015.
[20] X.J. Liu, et al., Simulation studies of divertor power exhaust with neon seeding for CFETR with GW-level fusion power, Phys. Plasmas 27 (2020), 092508.
[21] H. Si, et al., SOLPS-ITER simulations of high power exhaust for CFETR divertor with full drifts, Nucl. Fusion 62 (2022), 026031.
[22] S. Kwon, K. Im, S.-H. Hong, H. Lee, T.D. Rognlien, W. Meyer, K. Kim, Recent progress in the design of the K-DEMO divertor, Fusion Eng. Des. 159 (2020) 111770.
[23] T.D. Rognlien, M.E. Rensink, D.P. Stotler, Scrape-off layer plasma and neutral characteristics and their interactions with walls for FNSF, Fusion Eng. Des. 135 (2018) 380–393.
[24] M.E. Rensink, T.D. Rognlien, Plasma heat-flux dispersal for ACT1 divertor configurations, Fusion Sci. Technol. 67 (1) (2015) 125–141.
[25] R.A. Pitts, et al., Physics basis for the first ITER tungsten divertor, Nucl. Meter. Energy 20 (2019), 100696.
[26] R.A. Pitts, S. Carpentier, F. Escourbiac, T. Hirai, V. Komarov, S. Lisgo, A. S. Kukushkin, A. Loarte, M. Merola, A. Sashala Naik, R. Mitteau, M. Sugihara, B. Bazylev, P.C. Stangeby, A full tungsten divertor for ITER: physics issues and design status, J. Nucl. Mater. 438 (2013) S48–S56.
[27] N. Asakura, Recent Developments of Plasma Exhaust and Divertor Design for Tokamak DEMO Reactors, 25th International Conference on Plasma Surface Interactions in Controlled Fusion Devices (remote, Korea, 13–17 June 2022) MR01.
[28] M. Siccinio, et al., Figure of merit for divertor protection in the preliminary design of the EU-DEMO reactor, Nucl. Fusion 59 (2019), 106026.
[29] M. Kovari, et al., PROCESS: a systems code for fusion power plants-Part 2: engineering, Fusion Eng. Des. 104 (2016) 9.
[30] M. Nakamura, et al., Efforts towards improvement of systems codes for the Broader Approach DEMO design, Fusion Eng. Des. 87 (2012) 864.
[31] N. Asakura, et al., A simulation study of large power handling in the divertor for a Demo reactor, Nucl. Fusion 53 (2013), 123013.

[32] R. Wenninger, et al., Advances in the physics basis for the European DEMO design, Nucl. Fusion 55 (2015), 063003.
[33] Y.R. Martin, T. Takizuka, T.-M. Group, Power requirement for accessing the H-mode in ITER, J. Phys.: Conf. Ser. 123 (2008) 012033.
[34] A. Kallenbach, et al., Optimized tokamak power exhaust with double radiative feedback in ASDEX Upgrade, Nucl. Fusion 52 (2012), 122003.
[35] A. Kallenbach, et al., Partial detachment of high power discharges in ASDEX Upgrade, Nucl. Fusion 55 (2015), 053026.
[36] P. Pereslavtsev, et al., Neutronic analyses of generic issues affecting thetritium breeding performance in different DEMO blanket concepts, Fusion Eng. Des. 109–111 (2016) 1207–1211.
[37] N. Asakura, et al., Investigations of impurity seeding and radiation control for long-pulse and high-density H-mode plasmas in JT-60U, Nucl. Fusion 49 (2009), 115010.
[38] H. Utoh, et al., Studies of the plasma vertical instability and its control concepts in JA and EU broader approach, DEMO design activity, Fusion Eng. Des. 136 (2018) 874.
[39] A. Huber, et al., Comparative H-mode density limit studies in JET and AUG, Nucl. Metter. Energy 12 (2017) 100.
[40] A.S. Kukushkin, H.D. Pacher, G.W. Pacher, V. Kotov, R.A. Pitts, D. Reiter, Consequences of a reduction of the upstream power SOL width in ITER, J. Nucl. Mater. 438 (2013) S203–S207.
[41] T. Eich, et al., Scaling of the tokamak near the scrape-off layer H-mode power width and implications for ITER, Nucl. Fusion 53 (2013), 093031.
[42] A. Kallenbach, N. Asakura, A. Kirk, A. Korotkov, M.A. Mahdavi, D. Mossessian, G. D. Porter, Multi-machine comparisons of H-mode separatrix densities and edge profile behaviour in the ITPA SOL and Divertor Physics Topical Group, J. Nucl. Mater 337-339 (2005) 381–385.
[43] A.W. Leonard, et al., Compatibility of separatrix density scaling for divertor detachment with H-mode pedestal operation in DIII-D, Nucl. Fusion 57 (2017), 086033.
[44] T. Eich, et al., JET Contributors; Correlation of the tokamak H-mode density limit with ballooning stability at the separatrix, Nucl. Fusion 58 (2018), 034001.
[45] A. Loarte, Effects of divertor geometry on tokamak plasmas, Plasma Phys. Control. Fusion 43 (6) (2001) R183–R224.
[46] S. Qin, et al., Design analysis and remote handling compatibility for a CFETR long leg divertor concept, Fusion Eng. Des. 167 (2021), 112351.
[47] D. Reiter, The TRIM code surface database (http://eirene.de/trim.pdf) (2010).
[48] P.C. Stangeby, J.D. Elder, Calculation of observable quantities using a divertor impurity interpretive code DIVIMP, J. Nucl. Mater. 196–198 (1992) 258.
[49] P.C. Stangeby, The plasma boundary of magnetic fusion devices, IOP Publishing, 2000.
[50] A.V. Chankin, et al., Monte Carlo simulations of tungsten redeposition at the divertor target, Plasma Phys. Control. Fusion 56 (2014), 025003.
[51] F. Maviglia, G. Federici, G. Strohmayer, R. Wenninger, C. Bachmann, R. Albanese, R. Ambrosino, M. Li, V.P. Loschiavo, J.H. You, L. Zani, Limitations of transient power loads on DEMO and analysis of mitigation techniques, Fusion Eng. Des. 109-111 (2016) 1067–1071.
[52] S.I. Krasheninnikov, Reverse flow and parameter profiles in a dense tokamak divertor plasma, Nucl. Fusion 32 (1992) 1927–1934.
[53] G. Mazzone, J.-H. You, C. Bachmann, U. Bonavolontà, V. Cerri, D. Coccorese, D. Dongiovanni, D. Flammini, P. Frosi, L. Forest, G. Di Gironimo, G. Di Mambro, V. Imbriani, A. Maffucci, D. Marzullo, P.A. Di Maio, M.T. Porfiri, E. Vallone, R. Villari, E. Visca, C. Vorpahl, Eurofusion-DEMO divertor - cassette design and integration, Fusion Eng. Des. 157 (2020) 111656.
[54] J.H. You, et al., Divertor of the European DEMO: engineering and technologies for power exhaust, Fusion Eng. Des. 175 (2022), 113010.
[55] X.Y. Qian, et al., New designs of target and cooling scheme for water cooled divertor in DEMO, Nucl. Fusion 61 (2021), 036008.
[56] R. Villari, et al., Nuclear analysis of the ITER full-tungsten divertor, Fusion Eng. Des. 88 (2013) 2006.
[57] G. Federici, et al., Overview of the design approach and prioritization of R&D activitiestowards an EU DEMO, Fusion Eng. Des. 109–111 (2016) 1464–1474.
[58] H. Utoh, S. Kakudate, R. Hiwatari, Y. Someya, Y. Sakamoto, N. Asakura, S. Tokunaga, K. Tobita, Progress on reliability of remote maintenance concept for JA DEMO, Fusion Eng. Des. 146 (2019) 1583–1586.
[59] A. Hasegawa, et al., Neutron irradiation effects on tungsten materials, J. Nucl. Mater. 89 (2014) 1568–1572.
[60] Y. Ueda, et al., Baseline high heat flux and plasma facing materials for fusion, Nucl. Fusion 57 (2017), 092006.
[61] C.h. Linsmeier, et al., Development of advanced high heat flux and plasma-facing materials, Nucl. Fusion 57 (2017), 092007.
[62] A. Alfonso, et al., Thermal stability of a highly-deformed warm-rolled tungsten plate in the temperature range 1100–1250°C, Fus. Eng. Des. 98–99 (2015) 1924.
[63] M. Tokitani, et al., Fabrication of divertor mock-up with ODS-Cu and W by the improved brazing technique, Nucl. Fusion 57 (2017), 076009.
[64] S.A. Fabritsiev, S.J. Zinkle, B.N. Singh, Evaluation of copper alloys for fusion reactor divertor and first wall components, J. Nucl. Mater. 233-237 (1996) 127–137.
[65] S.A. Fabritsiev, A.S. Pokrovsky, Effect of high doses of neutron irradiation on physicomechanical properties of copper alloys for ITER applications, Fusion Eng. Des. 73 (1) (2005) 19–34.
[66] J.-H. You, et al., A review on two previous divertor target concepts for DEMO: mutual impact between structural design requirements and materials performance, Nucl. Fusion 55 (2015), 113026.
[67] Y. Someya, et al., Design study of blanket structure based on a water-cooled solid breeder for DEMO, Fusion Eng. Des. 98–99 (2015) 1872.
[68] S. Kwon, K. Im, J.S. Park, Thermo-hydraulic optimization study for a high heat flux unit of the K-DEMO divertor target, Fusion Eng. Des. 134 (2018) 68–73.
[69] M. Fursdon, J.-H. You, Towards reliable design-by-analysis for divertor plasma facing components—Guidelines for inelastic assessment (part II: irradiated), Fusion Eng. Des. 160 (2020) 111831.
[70] J.-H. You, M. Li, K. Zhang, Structural lifetime assessment for the DEMO divertor targets: design-by-analysis approach and outstanding issues, Fusion Eng. Des. 164 (2021) 112203.
[71] J.H. You, et al., European divertor target concepts for DEMO: design rationales and high heat flux performance, Nucl. Mater. Energy 16 (2018) 1.
[72] J.-H. You, et al., High-heat-flux technologies for the European demo divertor targets: State-of-the-art and a review of the latest testing campaign, J. Nucl. Mater. 544 (2021), 152670.
[73] F. Crescenzi, et al., Design study of ITER-like divertor target for DEMO, Fusion Eng. Des. 98–99 (2015) 1263.
[74] F. Domptail, et al., The design and optimisation of a monoblock divertor target for DEMO using thermal break interlayer, Fusion Eng. Des. 154 (2020), 111497.
[75] A.v. Müller, et al., Application of tungsten-copper composite heat sink materials to plasma-facing component mock-ups, Phys. Scr. T 171 (2020), 014015.
[76] M. Richou, et al., Performance assessment of thick W/Cu graded interlayer for DEMO divertor target, Fusion Eng. Des. 157 (2020), 111610.
[77] J.-H. You, A. Brendel, S. Nawka, T. Schubert, B. Kieback, Thermal and mechanical properties of infiltrated W/CuCrZr composite materials for functionally graded heat sink application, J. Nucl. Mater. 438 (1-3) (2013) 1–6.
[78] E. Tejado, A.v. Müller, J.-H. You, J.Y. Pastor, The thermo-mechanical behaviour of W-Cu metal matrix composites for fusion heat sink applications: the influence of the Cu content, J. Nucl. Mater. 498 (2018) 468–475.
[79] J.H. You, et al., High-heat-flux performance limit of the tungsten monoblock targets: Impact on armor materials and implications for power exhaust, Nucl. Mater. Energy accepted.
[80] M. Tokitani, Y. Hamaji, Y. Hiraoka, S. Masuzaki, H. Tamura, H. Noto, T. Tanaka, T. Muroga, A. Sagara, Deformation and fracture behavior of the W/ODS-Cu joint fabricated by the advanced brazing technique, Fusion Eng. Des. 146 (2019) 1733–1736.
[81] M. Tokitani, et al., Application of the advanced multi-step brazing for fabrication of the high heat flux component, J. Nucl. Mater. 538 (2020), 152264.
[82] M. Tokitania, et al., Advanced multi-step brazing for fabrication of a divertor heat removal component, Nucl. Fusion 61 (2021), 046016.